



Impacts of seismic resolution on fault interpretation: Insights from seismic modelling

Thea Sveva Faleide^{a,*}, Alvar Braathen^a, Isabelle Lecomte^b, Mark Joseph Mulrooney^a, Ivar Midtkandal^a, Aina Juell Bugge^c, Sverre Planke^{d,e}

^a Department of Geosciences, University of Oslo, Box 1047 Blindern, 0316 Oslo, Norway

^b Department of Earth Science, University of Bergen, Box 7803, 5020 Bergen, Norway

^c Lundin Energy Norway AS, Strandveien 4, 1366 Lysaker, Norway

^d Volcanic Basin Petroleum Research AS, Høyenhalld, Blindernveien 5, 0361 Oslo, Norway

^e Centre for Earth Evolution and Dynamics, University of Oslo, Box 1028 Blindern, 0315 Oslo, Norway

ARTICLE INFO

Keywords:

Faults
Statistical analyses
Interpretation uncertainty
Seismic imaging and resolution
Seismic modelling

ABSTRACT

Seismic mapping of subsurface faults is hampered by factors such as seismic resolution, velocity control for depth conversion and human bias. Here, we explore the challenges and pitfalls related to interpreting normal faults by comparing objective and subjective uncertainties. A panel of 20 interpreters, with different geoscientific backgrounds, interpreted faults in modern conventional (dominant frequency 40 Hz) and high-resolution P-Cable (dominant frequency 150 Hz) 3D seismic data from the Hoop area, SW Barents Sea. The interpretations created by the test-panel were sorted into 10 scenarios characterized by different fault geometries. These scenarios were explored with 2(3)D point-spread function based convolution seismic modelling to investigate the potential of seismic data to image detailed fault architectures. The results reveal that: (1) Statistical analysis shows considerable variations between manually picked faults. (2) Identifying the location of fault tips is challenging and smaller antithetic faults are rarely recognizable. (3) Uncertainties arise from masking of closely spaced fault segments even where displacement values are large, showing distorted reflection signatures of apparent extensional fault tip monoclines. The distortion is larger for conventional versus high-resolution data. (4) In the conventional and high-resolution seismic data the vertical resolution of closely spaced reflections and small offset faults is 20 m and 5 m, respectively. (5) The utilisation of high-resolution seismic data, combined with seismic modelling, add confidence to interpretation of conventional seismic data in the same area. We conclude that subsurface fault mapping with seismic data requires insight in objective uncertainties associated with the data. Automatic machine-learning fault interpretation is void of subjective bias but still hampered by objective limitations. Further, a risking workflow requires acknowledgement of uncertainties that are transferred to seismic based fault analysis techniques such as juxtaposition analysis, quantitative fault seal analysis, and fault stability analysis.

1. Introduction

Evaluation and characterization of CO₂ storage sites and exploration prospects require an understanding of faults that are critical to site integrity. Many techniques exist for risking faults related to prospects/traps, most relying on a 3D fault model derived from seismic interpretation. This fault model is rarely challenged regarding seismic interpretation uncertainty. Seismic data comes with limitations and interpretation pitfalls - both objective uncertainties related to the

dataset itself and subjective uncertainties related to human bias when conducting seismic interpretation. This study explores the challenges and pitfalls related to interpreting normal faults by comparing objective and subjective uncertainties, and addresses how these can be identified, resolved and minimized.

Faults are usually picked as two-dimensional lines (fault sticks; main bold lines in Fig. 1) or simple, discrete planes in 3D data compared to complex zones observed in outcrop geology (Fig. 1). Detailed fault architectural elements including segments, splays and lenses, and the

* Corresponding author.

E-mail address: t.s.faleide@geo.uio.no (T.S. Faleide).

<https://doi.org/10.1016/j.tecto.2021.229008>

Received 17 February 2021; Received in revised form 17 July 2021; Accepted 27 July 2021

Available online 30 July 2021

0040-1951/© 2021 The Authors. Published by Elsevier B.V. This is an open access article under the CC BY license (<http://creativecommons.org/licenses/by/4.0/>).

damage zones are commonly below seismic detection-levels. In seismic models, fault surfaces are created by linked two-dimensional fault sticks, which represent a single surface that is inconsistent with the characteristics of faults in outcrop (Fig. 1; e.g., Wibberley et al., 2008; Childs et al., 2009; Braathen et al., 2009). Further, the depth interval where faults are picked in seismic data dictates the resolution of the geological model and thereby the extracted details. Fault illumination and imaging are associated with significant constraints; larger faults are easier to identify than smaller ones due to larger throws and thereby larger offsets of seismic horizons (Misra and Mukherjee, 2018), whereas fault dip impacts as to what extent the fault plane can be imaged at all. There may however be additional information available in 3D seismic data, e.g. attributes such as variance and dip, which in cases can allow detection of faults and imaging of deformed rock volumes (Alaei and Torabi, 2017; Cunningham et al., 2019).

Uncertainty associated with seismic interpretation falls into two different categories, objective and subjective (Tannert et al., 2007). All interpretations host elements of both (Bond et al., 2007; Schaaf and Bond, 2019). Objective uncertainties relate to limitations of seismic data in terms of resolution and quality, imaging issues of complex subsurface geometries, as well as uncertainties in seismic velocities used for depth conversion (Bond, 2015; Schaaf and Bond, 2019). Even though seismic data have improved over the last 40 years (Fig. 2), there are still significant limitations in resolution that impact fault interpretation. On the other hand, subjective uncertainties or human bias hang on interpreter's fault-picks that will vary based on their experience and background as well as time invested into the task (Bond et al., 2007; Bond, 2015; Schaaf and Bond, 2019; Michie et al., 2021). Several studies have worked with geological uncertainties, interpretation and reasoning skills related to structural geology in 2D (e.g., Bond et al., 2007, 2011, 2012, 2015;

Freeman et al., 2010; Bond, 2015; Alcalde et al., 2017a, 2017b, 2017c) and 3D seismic data (Schaaf and Bond, 2019).

In this study, we explore how to identify, resolve and address uncertainties and pitfalls associated with fault interpretation. Objective uncertainties are investigated by utilising two seismic datasets, conventional and high-resolution P-Cable seismic data, with differing resolutions from the Hoop area, SW Barents Sea (Fig. 3). We also address subjective uncertainties associated with interpretation of two key seismic profiles from the 3D seismic data by comparing the fault interpretations from a test-panel consisting of 20 geoscientists with different geological and geophysical background. Notably, this is not a case study of the geological evolution of the Hoop area. There is a generic focus on imaging and detection of faults in seismic datasets having different resolution (both vertical and horizontal). The Hoop area is selected because of the unique seismic datasets and the existence of interesting structural and depositional features (faults and clinoforms) in the shallow subsurface where the high-resolution seismic data demonstrate their strength.

The comparison of fault-picks is complemented by 2(3)D point-spread function (PSF)-based convolution seismic modelling (Lecomte et al., 2015). The same type of seismic modelling has been previously explored based on outcrop-studies (e.g. Anell et al., 2016; Botter et al., 2017; Rabbel et al., 2018; Eide et al., 2018; Lubrano-Lavadera et al., 2018; Wrona et al., 2020), analogue models (Kjøberg et al., 2017) and numerical discrete element models (DEM; Botter et al., 2014, 2016). Such studies contribute to (1) increase confidence in seismic interpretation, (2) investigate the gap in scale between outcrop and seismic data, and (3) determine the importance of seismic imaging issues (e.g., seismic resolution and detectability, interference of reflections from closely spaced interfaces) for the outcome of subsurface geological

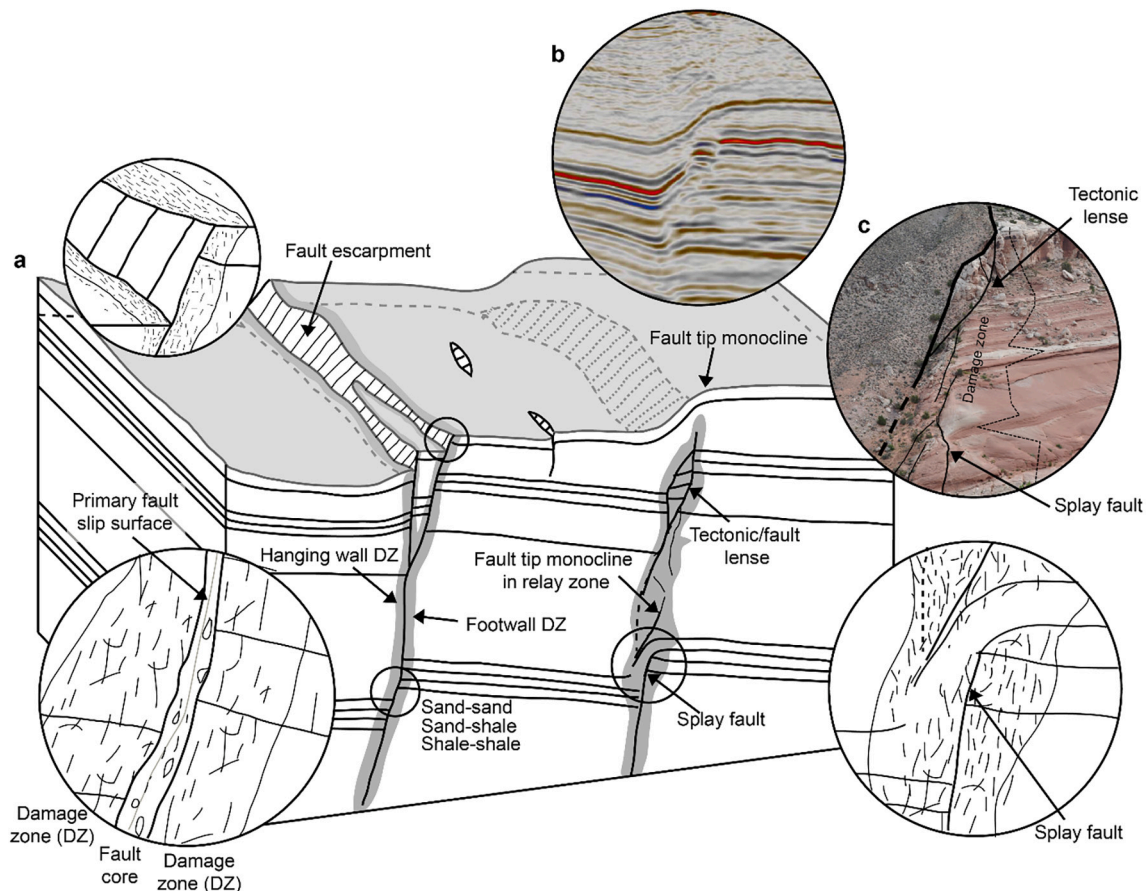


Fig. 1. (a) Schematic 3D fault-block model showing fault zones with various elements of the fault core and damage zone (DZ). (b) Fault in seismic data. Example from Hoop area, SW Barents Sea (this study). (c) Fault in outcrop. Example from Bartlett Wash Fault in Utah, USA (photograph is mirrored).

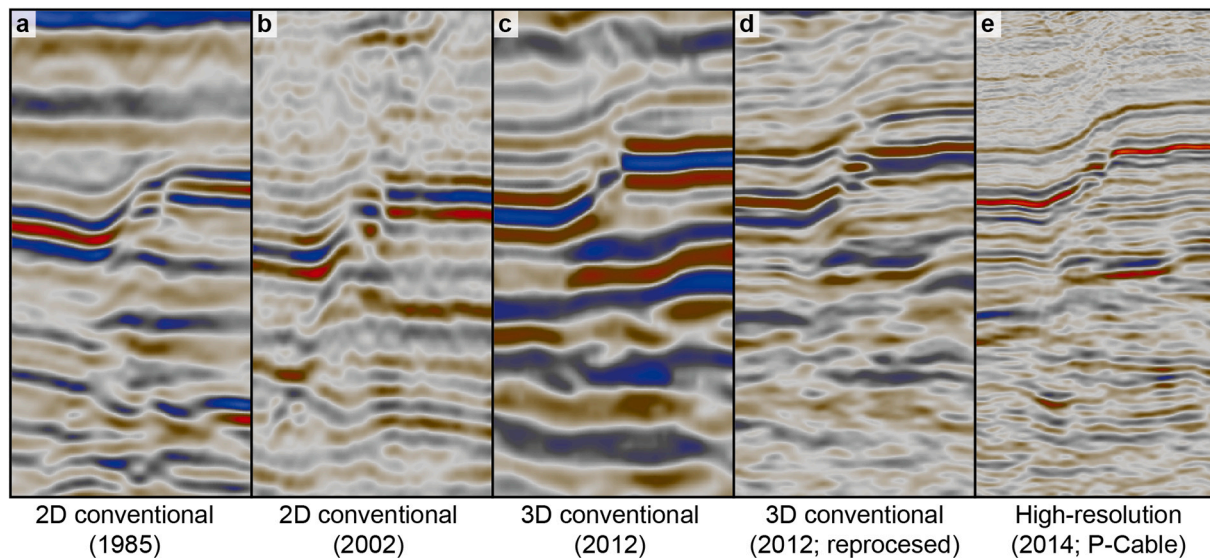


Fig. 2. Fault imaged in generations of seismic data for approximately the same location (all targeting one of the two main faults in this study, F1). From left to right: (a) 2D conventional seismic line from 1985, (b) 2D conventional line from 2002, (c) 3D conventional seismic from 2012 (dataset from Faleide et al., 2019), (d) reprocessed version of the same 3D conventional seismic with improved resolution and (e) seismic line in the 3D high-resolution (P-Cable) cube from 2014. Note that the two latter 3D seismic cubes are the dataset of this study. See Fig. 3 for location of the seismic lines. Seismic data in c-e courtesy of TGS, WGP and VBPR.

interpretations. With seismic modelling, we explore a statistical mean fault model and several models reflecting variability of different fault scenarios based on the interpretations from the test-panel. By means of this, we address (1) how resolution and illumination influence mapping of seismic faults, and (2) how high-resolution seismic data combined with seismic modelling can advise the interpretation of conventional seismic data.

2. Background

The dataset used in this study is centred on the NE-SW trending Hoop Fault Complex (HFC; Gabrielsen et al., 1990) in the SW Barents Sea (Fig. 3a,b). HFC is located in the transition between the Bjarmeland Platform to the east and deeper basins to the west (Fingerdjupet Sub-basin) and southwest (Maud Basin). The Hoop area is characterized by NNE-SSW and WNW-ESE fault sets (Collanega et al., 2017), of which two faults of the dominant NNE-SSW system are the focus of this study (faults F1 and F2; Fig. 3). The Hoop area has experienced several pulses of faulting. Three of these are of relevance to the stratigraphic interval studied here: (1) Middle Triassic, (2) Late Jurassic-Early Cretaceous and (3) Early Cretaceous (Gabrielsen et al., 1990; Fitriyanto, 2011; Collanega et al., 2017; Serck et al., 2017; Faleide et al., 2019).

2.1. Database

This study utilises the CFI_HFC 3D (2 ms HiRes) conventional seismic data and the overlapping HR14_3D_HFCE1 high-resolution P-Cable seismic volume, which both cover the area known as Gemini North (Fig. 3). The conventional 3D survey was acquired in 2012 by TGS and has a bin size of 12.5×18.75 m. We apply a reprocessed version of the 3D cube with 2 ms sampling resulting in improved resolution due to a broader frequency band compared to the 4 ms sampled data utilised in Faleide et al. (2019). The cube is cut at 2000 ms TWT for this study. The high-resolution (P-Cable) 3D survey was acquired in 2014 by TGS, WGP and VBPR, has a bin size of 4.7×6.25 m and extends down to 1150 ms TWT. Both conventional and high-resolution P-Cable seismic offer zero-phase polarity, and peaks corresponding to an increase in acoustic impedance are represented as red.

We utilize five exploration wells (Fig. 3), 7325/4-1 (Gemini North), 7324/6-1 (Sputnik), 7324/2-1 (Apollo), 7325/1-1 (Atlantis) and 7324/

3-1 (Intrepid Eagle), to obtain information on lithologies and physical properties based on geophysical logs, in addition to age and boundaries between the main formations/seismic sequences. The Gemini North well is the most important for this study since it is located inside the focus study area of overlapping conventional and P-Cable seismic volumes, and provides elastic parameters for the seismic modelling. We utilize the gamma ray log for lithology prediction, the sonic and density logs for 1D synthetic seismic traces, and time/depth relation of the well for seismic velocity estimations and depth conversion.

2.2. Seismic imaging and resolution

Since most normal faults at intermediate and shallow depths in sedimentary basins are rather steep, the fault itself is rarely imaged by seismic data. Instead, imaging is reliant on identification of reflection terminations and offsets, which in turn are dependent on seismic resolution. Seismic resolution is determined by the relationship between the interval velocity and the dominant frequency. Migration techniques applied also influence the final seismic resolution (Cartwright and Huuse, 2005). Velocity generally increases with burial depth due to mechanical and chemical compaction (Bjørlykke, 2015), whereas the frequency tends to decrease with depth as higher frequencies are more attenuated than lower ones (Brown, 2011). The combined effect is a decrease in resolution with depth.

The vertical resolution (limit of separability) for seismic data is a quarter of a wavelength ($\lambda/4$; Brown, 2011). The limit of visibility (Brown, 2011), or detectability, can vary depending on the seismic data quality. For data with a high signal-to-noise ratio, the limit of visibility can be as small as $\lambda/30$ (Brown, 2011). The horizontal resolution for good 3D migrated seismic data is about $\lambda/2$ (Herron, 2011). Bin size and trace spacing are of equal importance with respect to horizontal resolution, in addition to the survey aperture (Lebedeva-Ivanova et al., 2018). The horizontal resolution for (migrated) seismic data is therefore both frequency dependent ($\lambda/2$) and survey geometry dependent (Lebedeva-Ivanova et al., 2018).

P-Cable data typically have a vertical resolution of 3–7 m in the shallow subsurface (the upper about 500 m below the seabed), compared to 15–25 m in the conventional seismic data (Faleide et al., 2019). This is confirmed by studying the seismic data and the synthetic traces at the Gemini North well (Fig. 4). We use the average velocity in

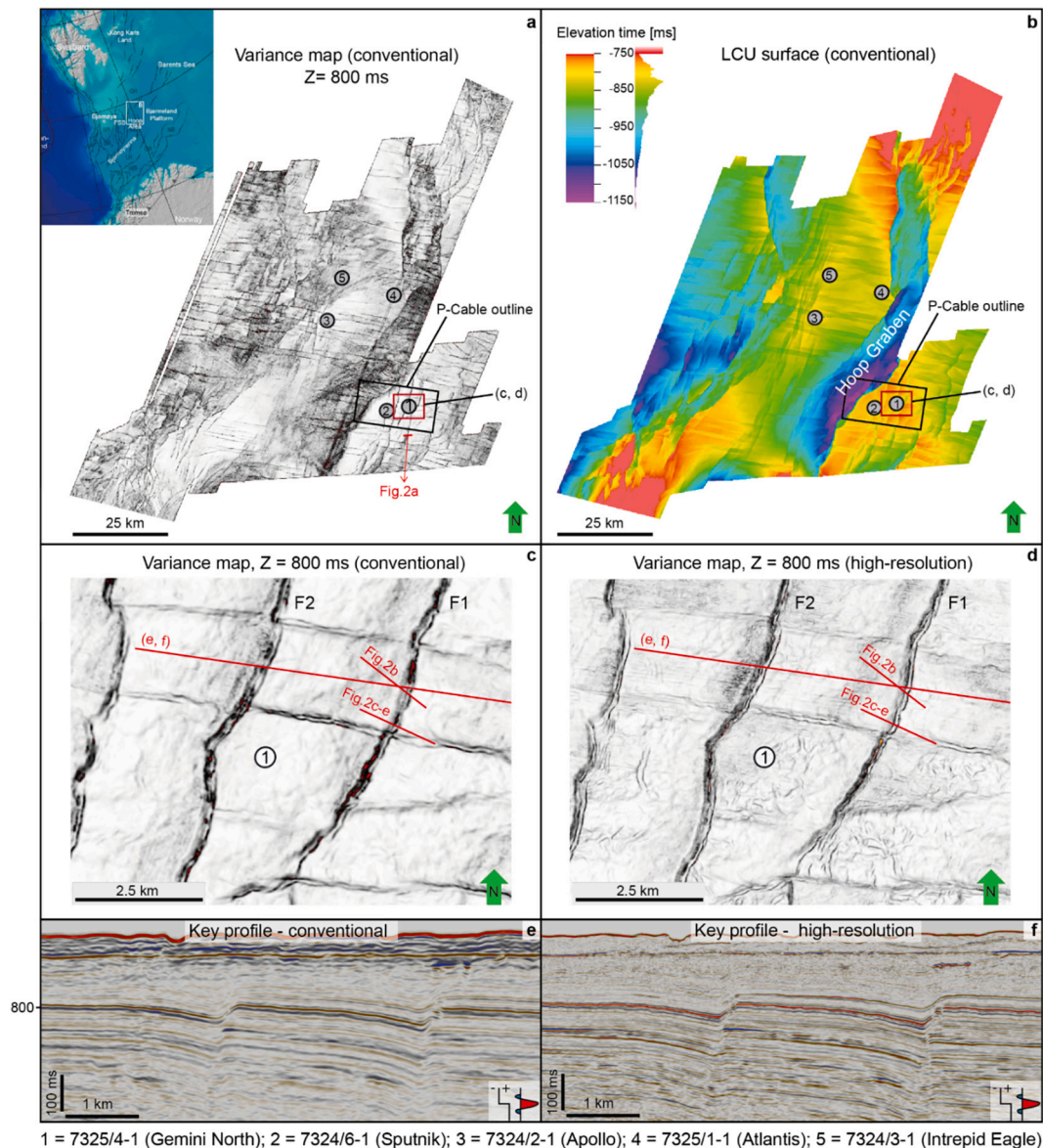


Fig. 3. Time-structure map of the Lower Cretaceous Unconformity (LCU), variance maps and location of key seismic lines shown in this paper. Location of wells are also marked. (a) Variance time slice at 800 ms in the 3D conventional seismic cube. The data coverage of this cube represents the study area. The location map in the upper left corner shows the study area, with reference to Svalbard and mainland Norway. (b) Time-structure map of the LCU horizon interpreted in the 3D conventional seismic cube. The outline of the 3D high-resolution seismic cube is marked as a black box in a and b. (c) Zoom in to the focus area (ref box in a and b) of the variance map (slice at 800 ms) in the 3D conventional seismic cube and (d) high-resolution seismic cube. Key WNW-ESE seismic profiles: (e) Uninterpreted conventional (arbitrary line) and (f) Uninterpreted high-resolution (inline). Profile locations are marked in c and d. F1 and F2 are the two main faults in the study, imaged in the seismic sections. Seismic data courtesy of TGS, WGP and VBPR.

the target depth interval from wells, and frequency from the power spectrum extracted from the seismic volume (Fig. S1.1 in supplementary material 1) to calculate the wavelength ($\lambda = v/f$; Herron, 2011).

3. Methods and workflows

The approach of this study is designed to meet the main aims; how to identify, resolve and address uncertainties and pitfalls associated with fault interpretation. Different methodologies are combined, and the main steps of the overall workflow are summarized in Fig. 5.

3.1. Seismic interpretation

The seismic interpretation part of the study includes three components: (1) One interpreter (the first author) performing a detailed 3D

seismic interpretation, in a focus area around the Gemini North well (Figs. 3 and 5a); (2) 20 geoscientists interpreting the same two seismic lines from each of the two seismic volumes manually on paper (Fig. 5b); and (3) automatic seismic interpretation on a limited area in the same two seismic data volumes (Fig. 5h). The combined results identify uncertainties, especially when considering individual interpreters.

A seismic-stratigraphic tie from the Gemini North well to the 3D seismic volumes is established utilising sonic and density logs (Fig. 4). The corresponding (1D) synthetic traces and their matching reflections for the Lower Cretaceous in the seismic data are correlated to the seismic stratigraphic framework in Faleide et al. (2019), which was mainly calibrated to the Apollo well (Fig. 3). The Jurassic and Triassic horizons are tied to formation tops in the Gemini North well (Norwegian Petroleum Directorate FactPages, 2021). The Lower Cretaceous Unconformity (LCU; Midtkandal et al., 2019) is mapped in both the conventional

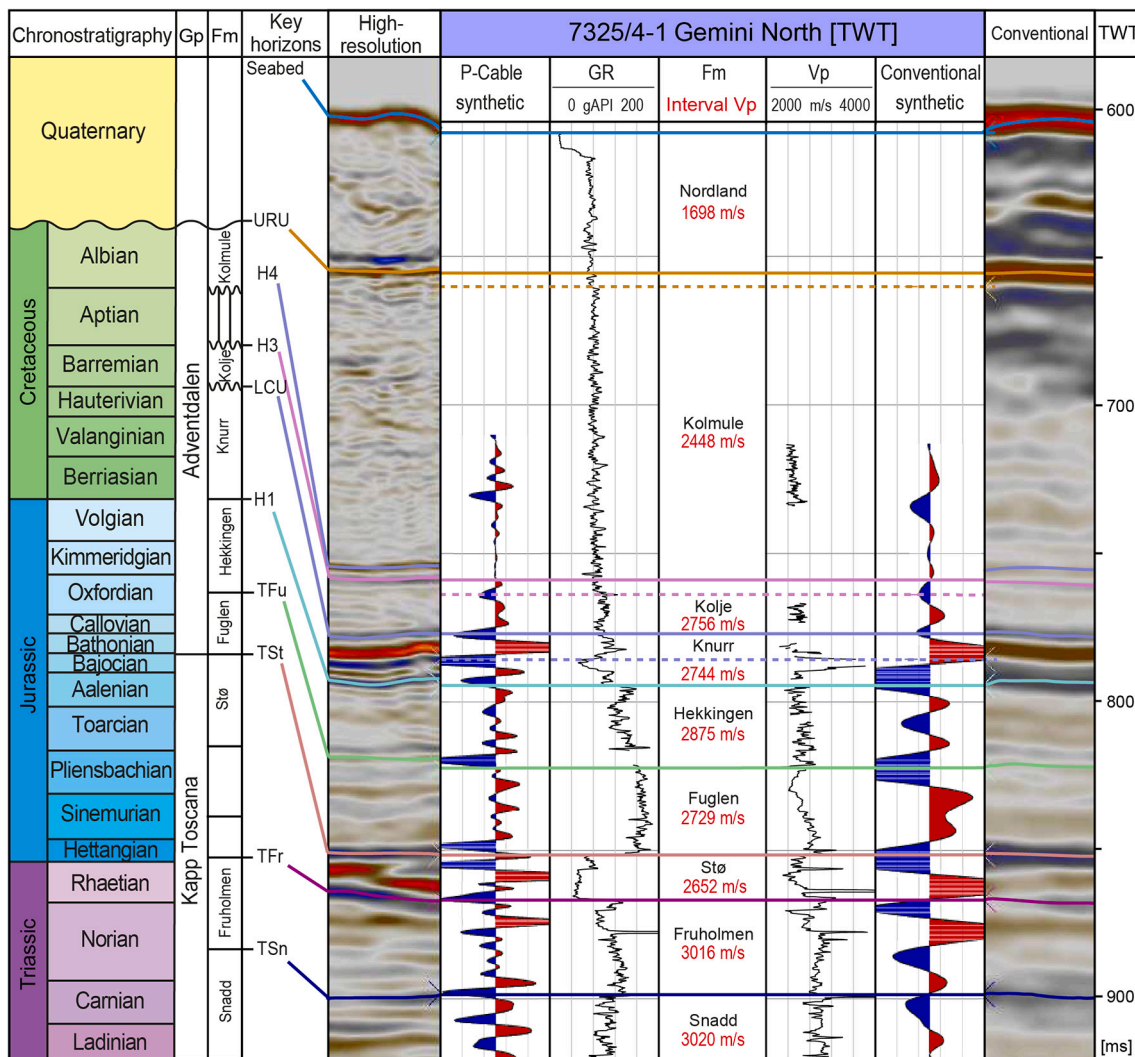


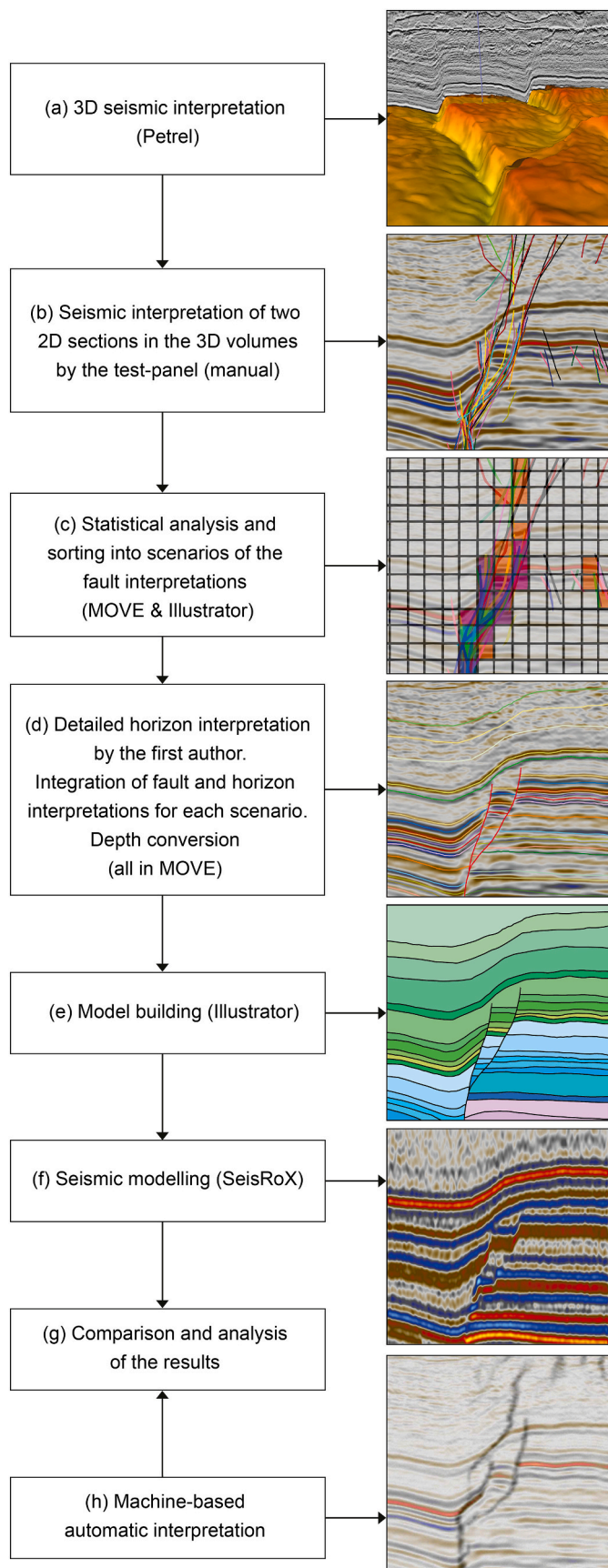
Fig. 4. Chronostratigraphic, lithostratigraphic and seismic stratigraphic framework of the Upper Triassic, Jurassic and Lower Cretaceous in the Hoop area in the SW Barents Sea, and comparison of P-Cable (left) and conventional seismic data (right) at the Gemini North well (7325/4-1). The seismic stratigraphic framework for Lower Cretaceous is based on and updated from the study of Faleide et al. (2019), and the Jurassic and Triassic framework is based on given depths of the formation tops in Gemini North well from the Norwegian Petroleum Directorate (NPD) FactPages. The well panel separating the seismic data includes gamma ray (GR), P-wave velocity (Vp), modelled synthetic traces for each seismic data type and the formations with their respective interval velocities. The formation boundaries are marked in the well data and correlated to corresponding reflections in the seismic data. We follow the solid purple line for the LCU reflection (Top Knurr) based on Faleide et al. (2019) and the stippled purple line represents the formation top of Top Knurr from NPD FactPages. Abbreviations: URU – Upper Regional Unconformity, LCU – Lower Cretaceous Unconformity, Fm – Formation, GP – Group, TFu – Top Fuglen, TSt – Top Stø, TFr – Top Fruholmen, TSn – Top Snadd. Seismic data courtesy of TGS, WGP and VBPR. (For interpretation of the references to colour in this figure legend, the reader is referred to the web version of this article.)

CFI_HFC 3D (2 ms HiRes) and high-resolution HR14_3D_HFCE1 seismic volumes and it highlights the structural elements in the Hoop area (Fig. 3b). We also perform a detailed fault and horizon mapping in a smaller area east of the Hoop graben (red box in Fig. 3a,b) in the high-resolution 3D data covering the Gemini North well and the location of the seismic lines used for the seismic modelling. Inlines and crosslines in the 3D cube are interpreted with varying increment (1, 5, 10 or 25) depending on continuity, strength, and structural complexity of the reflections.

Two main NNE-SSW trending faults, F1 and F2, are interpreted on each inline within the focus area (red box in Fig. 3). The faults are chosen since they bound the fault block hosting the Gemini North well, which provides the elastic parameters used in the seismic modelling. The seismic variance attribute, based on isolating edges and discontinuities from the input data set, as well as time-structure maps produced from seismic horizons are used to highlight the faults. These are used for

selection of the WNW-ESE oriented key profile (Fig. 3e,f), to be interpreted by the test-panel, based on the following criteria: (1) Crossing orthogonally both NNE-SSW faults, F1 and F2; (2) Parallel to and staying away from the minor WNW-ESE faults (Fig. 3c,d); (3) F1 and F2 should have different seismic expressions to challenge the test-panel.

To test subjective uncertainties related to seismic interpretation of faults the panel of 20 geoscientists manually interpreted the same 2D seismic time-section (vertical exaggeration x 5) selected from both the conventional and high-resolution 3D volumes (Figs. 3e,f and 5b). The test-panel members have different background (structural geologists, sedimentologists and geophysicists) and level of experience/expertise (PhD, post doc., professors and industry professionals). They traced the faults over a period of 20 min for each seismic section. This task was first conducted using the conventional seismic section and then repeated for the high-resolution seismic section. The interpreters could not refer to the first section when interpreting the second, in order to limit the bias



(caption on next column)

Fig. 5. Overall workflow of this study. (a) 3D seismic interpretation covering the larger Hoop area (see location in Fig. 3a,b). (b) Manual seismic interpretation by a panel of 20 interpreters. (c) Statistical analysis and sorting into scenarios of the fault interpretations. (d) Seismic horizon interpretation by the first author. Integration of the fault and horizon interpretations, and these are further depth-converted. (e) Building the geological model. (f) Seismic modelling. (g) Comparison and analysis of the results. (h) Machine-based automatic interpretation, compared to synthetic and actual seismic sections. See text for more details.

by comparing datasets. The task was to focus on structural interpretation (faults), while the horizons were interpreted later by the first author adjusting the interpretation to the fault picks from the test-panel.

One way to minimize the subjective uncertainty in fault interpretation is to apply fully data-driven fault identification. A variety of data-driven or data-assisted fault interpretation methods exists (e.g. Bahorich and Farmer, 1995; Hale, 2013), and recently, machine learning has proven to be a popular choice for automatic fault identification (Huang et al., 2017; Zhao and Mukhopadhyay, 2018; Wu et al., 2019). Here, we include a synthetic pre-trained machine learning model as interpreter #21 (Fig. 5h). This fault pick (#21) is compared to the manual picks of interpreters #1–20. The machine learning model was trained on a few hundred synthetic volumes, with both planar and listric fault examples, where each training cube of 128x128x128 pixels included 2–6 faults, and the model was trained with a U-Net-shaped 3D fully convolutional neural network (Ronneberger et al., 2015). This approach, using a synthetically trained neural network for automatic fault identification was first proposed by Wu et al. (2019). Because of the variability in the synthetic data used to train the model, the model is generic and not fine-tuned to one specific dataset or case study. Hence, the same trained model is applied to both the conventional and the high-resolution datasets described in this paper.

3.2. Seismic modelling

Seismic modelling is a valuable tool linking geological models and seismic images, hence relationships between geology and seismic response. Modelling results may guide seismic interpretation helping the interpreter to separate real structures from seismic artefacts (e.g., Botter et al., 2014, 2016; Lecomte et al., 2015, 2016; Anell et al., 2016).

Seismic modelling can be carried out in different ways. The simplest method of making synthetic seismic is by 1D convolution, which is a standard technique used for well-to-seismic tie in interpretation tools (Mondol, 2015; Lecomte et al., 2016). 1D synthetic seismograms have large uncertainties and limitations in geologically complex areas since the 1D approach does not take lateral velocity variations into account (Botter et al., 2014; Lecomte et al., 2016). A more ideal and valid approach with the potential of resolving geological details is to perform full-wavefield modelling, in which complete synthetic seismograms are generated based on solutions of the differential wave equation by a finite difference approach (Lecomte et al., 2015, 2016). However, this advanced technique is time-consuming and cannot be carried out on a routine base.

2(3)D PSF-based convolution modelling, a prestack depth migration (PSDM) simulator, offers an efficient and flexible intermediate option and can be performed both ray-based (e.g., Botter et al., 2014) and by a simple version using a generic filter, based on a few key parameters, to obtain the PSF (Botter et al., 2014; Lecomte et al., 2015, 2016). The 2(3) D PSF-based seismic modelling still uses the convolution principle but goes beyond a 1D approach, for which the wavelet is the sole element of the convolution operator, by using instead a 2(3)D convolution operator, i.e., the PSF (Lecomte et al., 2015, 2016). This is more realistic than 1D convolution as it considers model and survey dependent 2(3)D resolution and illumination effects, including diffraction energy. The method results in a better modelling of complex structures, especially when full-wavefield modelling is not affordable. PSF-based convolution

modelling allows geologists to better understand seismic images in relation to the input geomodels, analyse them and possibly improve their interpretation, thus being more critical in their conclusions (Botter et al., 2014, 2016; Lecomte et al., 2015; Anell et al., 2016). This modelling approach has recently been applied to fault models with promising results (Botter et al., 2014, 2016; Lecomte et al., 2015; Wood et al., 2015; Mascolo and Lecomte, 2020).

3.2.1. Model building

An important and time-consuming step of the seismic modelling workflow is to build the 2D geological models (Fig. 5e). All interpretations are scanned and imported as images into the interpretation software (e.g., MOVE; Fig. 5c,d), in addition to SEG-Y files for the two overlapping seismic lines. The original seismic lines are geo-referenced in this software – this allows transfer of the fault and horizon interpretation back to a seismic interpretation software (e.g., Petrel). Each interpretation is scaled correct to the seismic lines, and the fault interpretations are traced over and defined as individual fault set (one set for each interpreter) by the first author. The fault sets are connected to the original seismic lines (imported SEG-Y), for both the conventional and high-resolution seismic and their interpretations. The scanned images are hidden and only the fault sets (digital version of the fault interpretation by each interpreter), which now have the correct coordinates, remain and they can be ticked off and on to the seismic

profiles when performing the analysis.

A simple density statistical study is utilised on both key profiles with all 20 interpretations, counting how many single fault interpretations (2D fault sticks) that goes through or terminate inside each 3*3 mm squares in a grid covering the complete seismic line (Fig. 6c,d). The number of fault picks are divided into colour intervals (Fig. 6e,f). A statistical mean fault model is constructed based on the colour-coded statistics for the interpretations of the high-resolution seismic data (Fig. 6f).

In areas 1 and 2 (Fig. 6b), all interpretations of the high-resolution seismic data are sorted into different variability scenarios based on fault interpretation similarities (Fig. 7; Figs. S2.1-S2.3 in supplementary material 2). For each scenario, a hybrid fault interpretation is made based on all interpretations grouped into this (Fig. S2.3 in supplementary material 2). Finally, the horizons are traced by the first author and adjusted to the faults (Figs. 5d and 7). The horizon tracing varies a bit from each scenario since it is constrained by the fault interpretation. The mapped horizons and faults are depth-converted according to the two-way-travel time (TWT) and average velocity information from the Gemini North well (Fig. 5d). The depth-converted horizons and faults are exported as an image and imported to a graphics program (in an artboard with a reasonable pixel size relative to the size of the model; preferable 1 px = 1 m, corresponding to 1 m sampling) where they are converted to editable traces. Each layer is assigned a colour indicative of

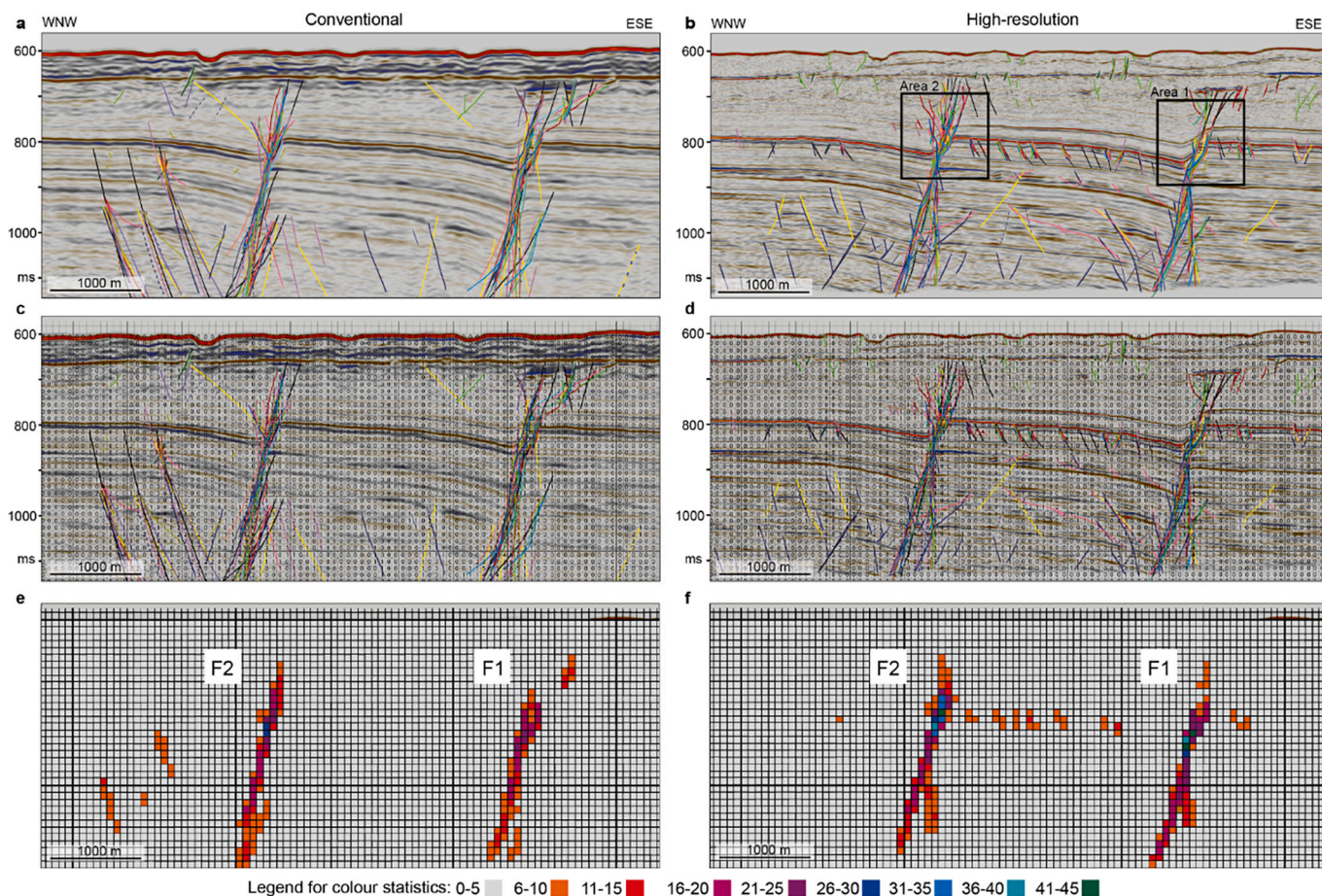


Fig. 6. Interpretation and statistical analysis of the WNW-ESE seismic lines of conventional and high-resolution seismic data covering the same line location. Uninterpreted seismic lines in Fig. 3e,f. (a) All interpretations done by the 20 interpreters on the conventional seismic line and (b) on the high-resolution seismic line. Each interpreter has its own colour, and these are the same for both seismic data types. Statistics for the conventional seismic line (c) and high-resolution seismic line (d). (e) Colour-statistics result of the interpretation on the conventional and (f) high-resolution seismic line. To see trends in the interpretations, the count of fault traces are grouped into intervals, where 0–5 is neglected, 6–10 is orange, 11–15 red, 41–45 green, etc. The statistics guides the mean fault model (of all interpretations) tested out in the seismic modelling. Seismic data courtesy of TGS, WGP and VBPR. (For interpretation of the references to colour in this figure legend, the reader is referred to the web version of this article.)

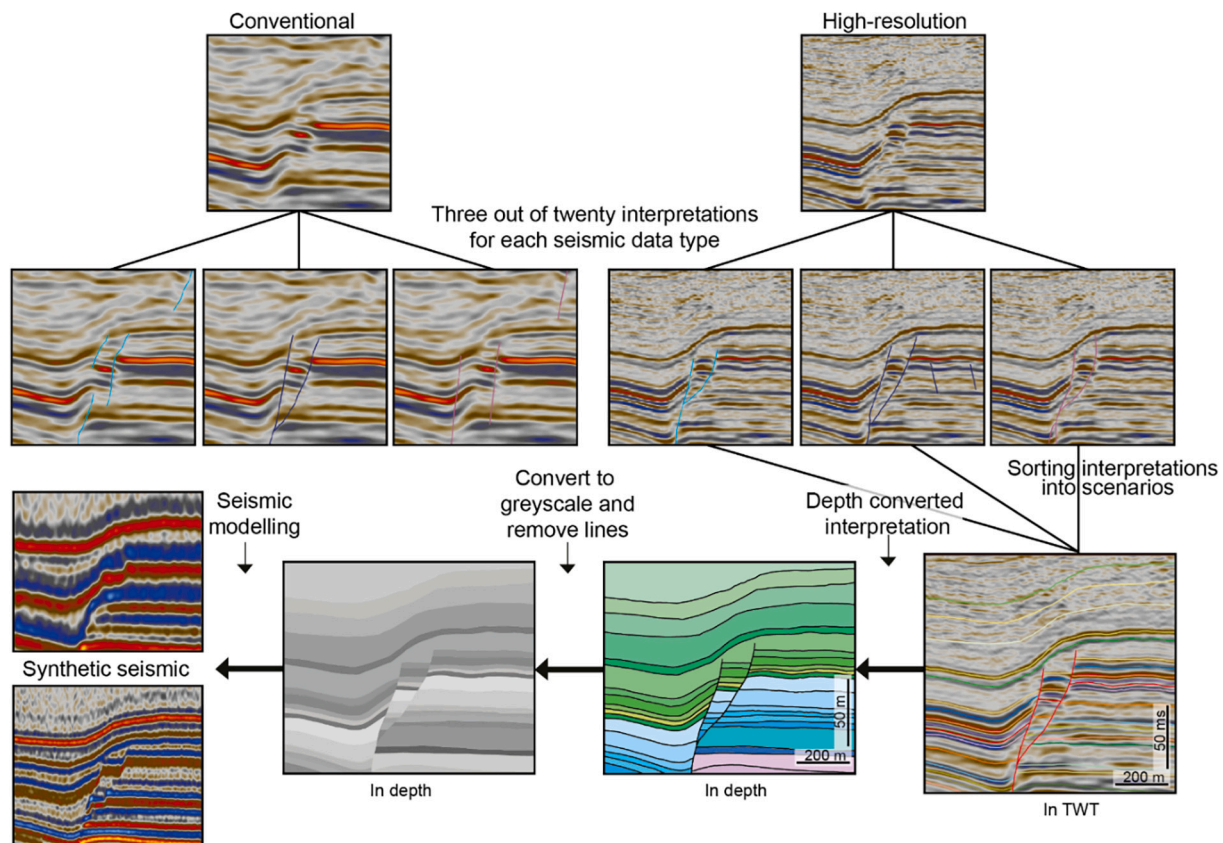


Fig. 7. Workflow for construction of the geological models. Sorting into scenarios and building of corresponding geological models are based on the high-resolution interpretations. The interpreted structures include important reflections that can be correlated across the faults. The fault and horizon interpretations are depth-converted according to the well information (relation between average velocity and TWT). Then each unit, bounded by two reflections is assigned a colour. The seismic modelling results show how the geological models are represented in a seismic image with wavelet (dominant frequency) corresponding to conventional and high-resolution data. See text for details. Seismic data courtesy of TGS, WGP and VBPR.

geological age. Since faults are often represented in seismic data by displacement of layers/reflections, and not the fault plane itself, fault picks are removed. The resultant model is exported as a PNG file, ready for input to the seismic modelling software (Figs. 5f and 7).

3.2.2. PSF-based convolution modelling

The main steps of the workflow for the PSF-based convolution seismic modelling are presented in Fig. 8. A 2D geological model is created from depth-converted horizon and fault interpretations. This model is exported as a PNG image, assigned constant elastic parameters (V_p , V_s , density) for each layer and converted to SEG-Y file format. The SEG-Y files are imported into the seismic modelling software. A reflectivity model (Fig. 8d) is first generated from the geological model and elastic parameters using the Zoeppritz equations (Shuey, 1985). We use a simplified version of the PSF-based convolution modelling by designing PSFs from a few key parameters (Lecomte et al., 2016). An equivalent PSDM filter is generated based on a generic illumination pattern defined by a regular illumination of all reflector dips until a selected maximum (e.g., 0°–45° dip range), an average velocity calculated from the well data, incident angle based on survey geometry (typical offsets), and wavelets extracted from the seismic data. The PSF is obtained from a Fourier Transform (FT) of the PSDM filter (Fig. 8e) and convolved with the reflectivity model to obtain a synthetic (PSDM-like) seismic image (Lecomte et al., 2015, 2016). The synthetic seismic image (Fig. 8f) of the input geological model can be analysed as function of various wavelets, and the different parameters mentioned earlier.

Geophysical parameters such as illumination angles, incident angle, wavelets, and elastic parameters affect the outcome of the modelling, i.e. the synthetic seismic data. Variations in geophysical parameters are

tested by different wavelets and incident angles representative of both the conventional and high-resolution seismic volumes. By varying the wavelets, hence the dominant frequency and bandwidth, for the same geological model, different resolutions of the synthetic seismic data become available. Wavelets are extracted from both seismic datasets with different time-windows: interval 700–900 ms TWT, complete vertical window (600–1150 TWT), and each 100 TWT interval (650–750, 750–850, etc.). The representative dominant frequencies in the study area for conventional and high-resolution seismic data are 40 Hz and 150 Hz, respectively (Fig. S1.1 in supplementary material 1). For the target areas around F1 and F2, the dominant frequencies are 40–45 Hz and 90 Hz, respectively (750–850 TWT interval; Fig. S1.1 in supplementary material 1). A 45° illumination angle is used, meaning that reflectors having dips between 0 and 45° are illuminated. The incident angle for the long-offset conventional seismic data is set to 20°, while 0° is used for the short-offset high-resolution seismic data (Fig. S1.1 in supplementary material 1). The elastic parameters, V_p , V_s and density, for the geological models are summarized in Table S3.1 in supplementary material 3.

The synthetic seismic sections become more realistic by adding some noise. A coloured-noise model is here generated by convolution of a random white reflectivity model with the same PSF used for the synthetic seismic described earlier, thus reproducing the same (PSDM-like) filtering effect that the geological models have in the seismic modelling. The noise model reflectivity range is scaled according to the reflectivity range of the input geological model in order to examine a spectrum of signal-to-noise ratios. All synthetic seismic sections, included the noise components, are also amplitude-calibrated so that an isolated peak of strength +1 in reflectivity will correspond to a peak of amplitude +1 in

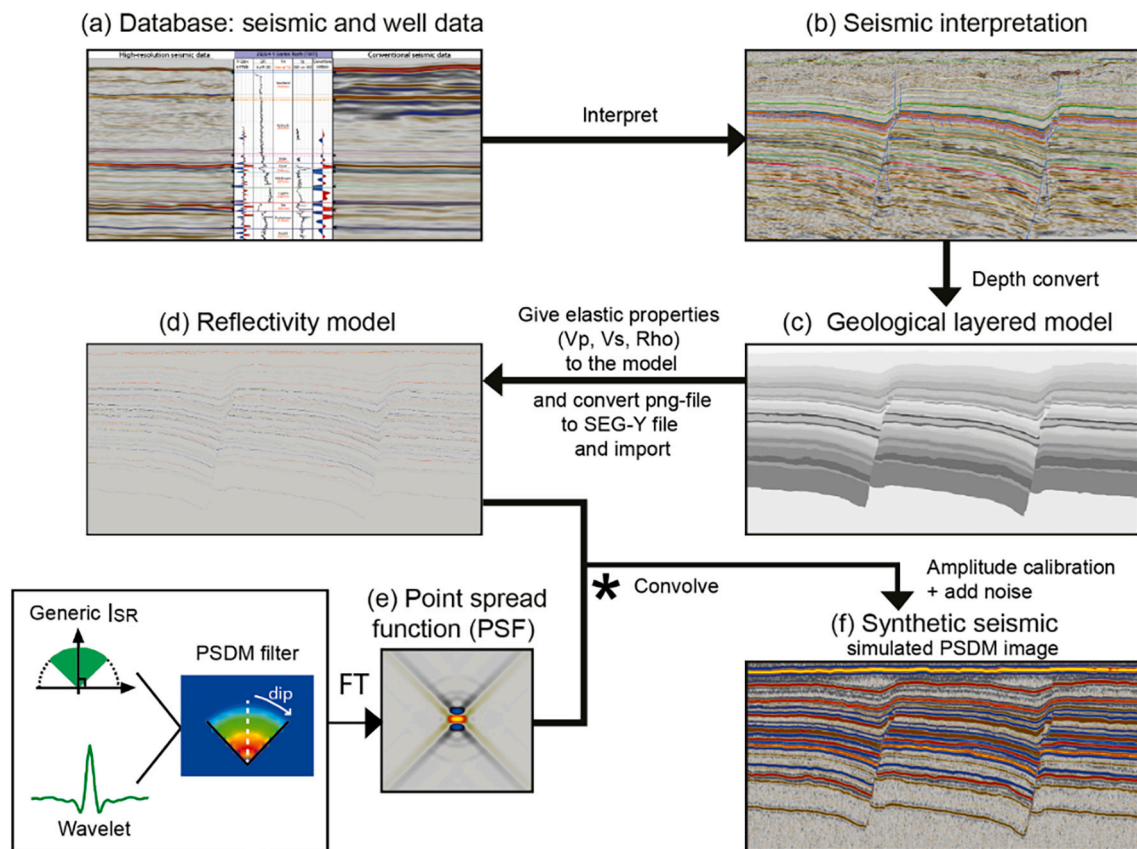


Fig. 8. Workflow for the seismic modelling. The database (a) consists of post-stack 3D seismic in time and well data. First step is interpretation of the seismic data (b). A geological layered model (c) is created based on depth-converted interpretations. The geological layered model (in depth) is exported as a png file in grey scale, given elastic parameters, and converted to SEG-Y files through a matlab-script. A reflectivity model (d) is convolved with a point-spread function (PSF) (e) and the output of the seismic modelling is the synthetic seismic image (f). See text for details. Seismic data courtesy of TGS, WGP and VBPR.

the calibrated seismic. Difference plots are a powerful tool for comparison and detection of differences in synthetic seismic sections. They can detect the differences between the fault scenarios, and how the fault and horizon interpretation affect the seismic imaging.

4. Results

4.1. Seismic interpretations

Faults in the study area are visible in the time-structure map of the Lower Cretaceous Unconformity (LCU) derived from conventional seismic data (Fig. 3b). The variance cube highlights the faults in the area at 800 ms (Fig. 3a,c-d). A broader regional extent of faults can be observed in the conventional 3D that covers a larger area, where the major Hoop graben changes from a N-S orientation in the north of the area to a NE-SW orientation farther south (Fig. 3b). Faults sets showing N-S, NE-SW, NNE-SSW and WNW-ESE trends are imaged, including the Hoop graben and its bounding faults. The selected WNW-ESE seismic sections, orthogonal to faults F1 and F2, are located c. 1.7 km from the Gemini North well (Fig. 3c-f). The fault throw is largest at the level of the Triassic units and decreases up-section (Fig. 6). F1 has average throws of 55 m within the Triassic, 41 m in the Jurassic and 21 m in the Lower Cretaceous units. Corresponding values for F2 are 50 m, 35 m and 17 m, respectively.

The fault picks of all 20 interpreters identify the main faults F1 and F2 (Fig. 6). The conventional 3D data generally show more interpretation uniformity. Both F1 and F2 are segmented, and minor individual faults (e.g., z interval 800–850 ms) are traced in the high-resolution data (Fig. 6b). In deeper parts of the sections ($z = 850\text{--}1000$ ms), the

interpretations of F1 and F2 are more consistent within each dataset compared to in the upper part ($z = 675\text{--}850$ ms). The latter relates to up-section plays that offer more options in picking for shallow parts of F1 and F2, which is highlighted in the scenario models presented in Chapter 4.2.2. Picking of minor faults varies in the two seismic data types, and the dip direction of the picked faults are less consistent in the high-resolution than in the conventional seismic. For the conventional data, antithetic faults were picked in the hanging wall of F2, while fault segments in the Upper Jurassic-Lower Cretaceous in between F1 and F2 are only suggested for the high-resolution data (Fig. 6e,f).

The automatic interpretation results from the pre-trained machine-learning model (Fig. 5h) show that most key elements of fault segments are identified in the high-resolution seismic data (Fig. 9e,f). Segments F1a and F1b are clearly detected and traced (Fig. 9f), rather similar to the mean interpretation (Fig. 9d). However, there are also some striking deviations between the manual (interpreters #1–20; Fig. 9a-b,i-j) and the automatic (#21; Fig. 9e-h) fault interpretations. The segments merge at a slightly shallower level than in the mean interpretation of the test-panel. F1a cuts H4 and terminates just above this horizon. Above F1b, a fault segment has been traced that merges with the monocline at H4 level. It cuts across H4 in the lower part of the monocline and continues downwards without a clear link to F1b. The deeper part of F1 appears even steeper than in the mean interpretation by the test-panel. The automatic interpretation of F2 in the high-resolution seismic is more segmented vertically (Fig. 9e). Fault segments F2a and F2b do not link. F2b is traced up-section well above H4, clearly offsetting this horizon. Further, the F2a segment is not traced as far up as in the mean interpretation of the test-panel, but cuts H4.

The automatic interpretation of the conventional seismic data

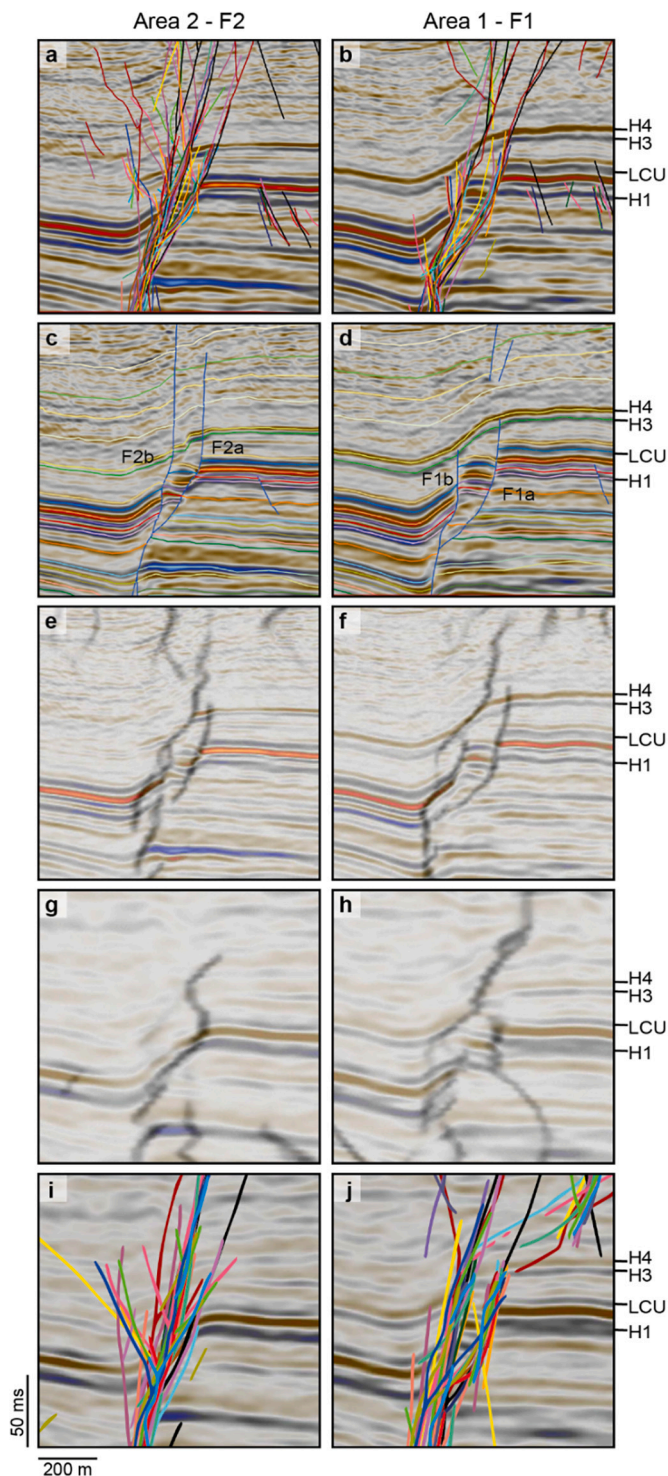


Fig. 9. Comparison of the machine-based automatic interpretations with the manual fault picking of F1 and F2 by the test-panel. (a,b) All twenty interpretations on top of the high-resolution seismic data. (c,d) The mean fault model based on the colour-code density statistics (Fig. 6f). Interpreter #21, results of a synthetically trained neural network (AI-model) blended on top of the high-resolution (e,f) and conventional (g,h) seismic data. The synthetic training data are generated by Lundin Energy Norway and include synthetic seismic data generated with different random reflectivity series, wavelets, frequency content, noise, and with different fault architectures such as planar, listric and intersecting faults. (i,j) All 20 interpretations on top of the conventional seismic data. Seismic data courtesy of TGS, WGP and VBPR.

(Fig. 9g,h) is unable to catch the same level of detail as described for the high-resolution seismic data. For F1 (Fig. 9h), the shallow fault segment above H4 is identified in a rather similar fashion. It appears that the conventional data lack the horizontal resolution needed to resolve the relationships between segments F1a and F1b. The automatic interpretation tries to delimit the fault block between F1a and F1b but with limited success. For F2 (Fig. 9g), the interpreted fault segment above H4 makes a strange bend before it interferes with the monocline at H4 level. There is no linkage with deeper segments of F2, and segment F2a is not identified. Compared to the automatic picks mentioned above, there are however large variations in the interpretations of the conventional data by the test-panel (Fig. 9i,j).

4.2. Geological models and synthetic seismic

Several queries around validity of fault picks are explored by the synthetic seismic testing of scenario-based models. Three different test populations are included: (i) one statistical mean fault model covering the whole seismic section; (ii) four scenarios based on variability in a limited area of F1; and (iii) five scenarios based on variability targeting parts of F2 (Fig. 6b). The 2D geological models are based on the high-resolution seismic data since this dataset provides better imaging, hence details, of the actual geology.

4.2.1. Statistical mean fault model

The statistical mean model (Fig. 10b), 7 km wide and 450 m high (with 0–450 m as the depth range of the model), consists of 34 layers with individual elastic parameters (Table S3.1 in supplementary material 3) and includes sedimentary strata from the Middle Triassic to Quaternary. The mean fault model of F1 and F2 suggests they split into two segments below c. 175 m, where they display a hard-linked antithetic fault in the footwall of the main segment (Fig. 10a,b). The interpreted antithetic fault is likely an artefact caused by poor imaging in a shadow zone in the footwalls of F1 and F2. This interpretation pitfall will be discussed later in the context of both objective and subjective uncertainties. Interpretations shallower than c. 175 m suggest that two fault segments occur between 100 and 175 m in F1 (F1a,b) and 50–175 m in F2 (F2a,b). Minor synthetic and antithetic faults occur in between the two main faults. Segments F1a and F1b terminate below horizon H4, whereas two minor isolated fault segments occur in the H4-URU interval. For F2a and F2b minor offsets of H4 and the horizons above are apparent. Both segments terminate below URU.

The synthetic seismic sections emphasize the importance of resolution in the two seismic datasets (Fig. 10c,d). In the conventional synthetic section (Fig. 10c), reflections from closely spaced interfaces interfere, making it impossible to resolve individual thin layers with typical thickness of 5–10 m, for instance at label 1. In the high-resolution synthetic section (Fig. 10d), individual layers are better resolved and more interfaces can be identified. F1a can be traced farther up-section, perhaps all the way up to the two minor isolated fault segments in the H4-URU interval (label 2; Fig. 10c). There, due to the lower dominant frequency, the conventional synthetic seismic section masks some of the layers/interfaces. For the high-resolution synthetic section, F1 clearly terminates below H3 (label 2; Fig. 10d), consistent with the statistical mean fault model (Fig. 10b). In deeper parts of F1 and F2, the fault plane itself is imaged in both the conventional and high-resolution synthetic sections (label 3; Fig. 10c,d). The down-faulted block in F1, between F1a and F1b, is visible in both synthetic sections but appears more distinctly layered in the high-resolution synthetic seismic (label 4; Fig. 10c,d). Similarly, the fault block between F2a and F2b (label 5; Fig. 10c,d) is more layered and isolated in the high-resolution synthetic seismic section. The minor antithetic and synthetic faults (at depth interval 125–155 m) in between F1 and F2 are only imaged in the high-resolution synthetic seismic section, as these are largely below the seismic resolution of the conventional seismic data (label 6; Fig. 10c,d).

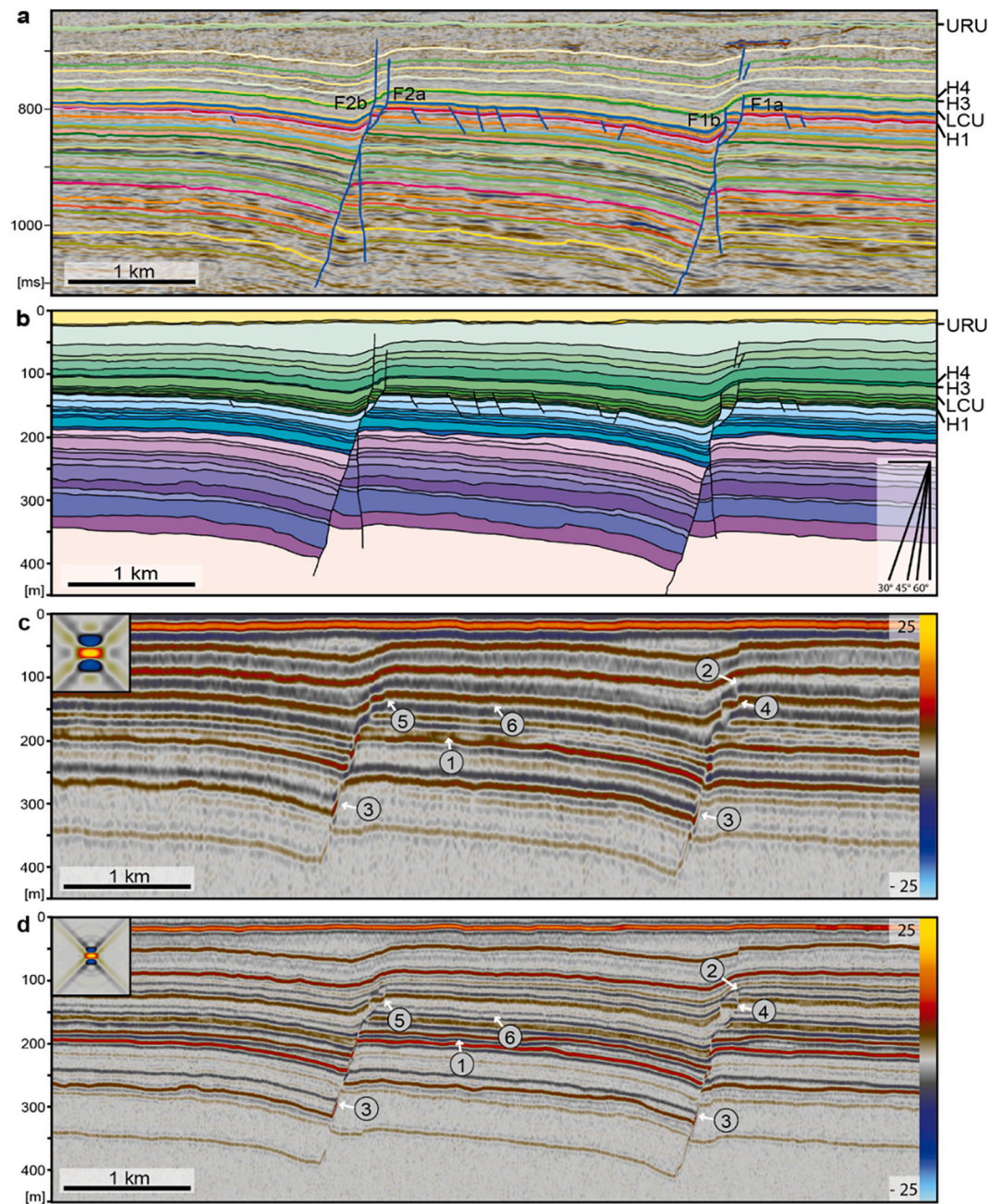


Fig. 10. The mean fault model. (a) The mean fault interpretation based on the colour-code density statistics and with 32 horizons traced and correlated across the faults. (b) The statistical mean fault model in depth (the colour represents the age of the unit: purple/pink = Triassic, blue = Jurassic, green = Cretaceous and yellow = Quaternary). The 34 layers each have individual elastic properties (P-wave velocity, S-wave velocity and density; see Table S3.1 in supplementary material 3). (c) Conventional synthetic seismic section and (d) high-resolution synthetic seismic section. The numbered labels point out key observations described in the text. The vertical exaggeration (VE) is 5 for the synthetic seismic sections, while the PSF's are shown with VE = 1. See text for more details. Seismic data courtesy of TGS, WGP and VBPR. (For interpretation of the references to colour in this figure legend, the reader is referred to the web version of this article.)

4.2.2. Scenario models for F1 and F2

Uncertainty in picking of the two faults, F1 and F2, can be further explored in scenarios sorted based on varying fault geometries interpreted by the test-panel (Figs. 11 and 12; Fig. S2.3 in supplementary material 2). In areas with the largest variation in fault interpretations, hence largest subjective uncertainties (area 1 and area 2; Fig. 6b), scenarios were established based on variability and sorting into groups of similar fault geometries. Area 1, covering F1, is divided into four scenarios (Fig. 11) and area 2, covering F2 is divided into five scenarios (Fig. 12). Common to all scenarios is that they have significant geometric overlaps but offer slight variations in fault picks, for instance

open or broken relay zones. Horizon picks vary inside complex fault geometries, where fault interpretations dictate how the horizons are traced. The scenario models for F1 and F2 are 950 m wide and 160 m high, and consist of 21–22 layers (Table S3.1 in supplementary material 3) covering sedimentary strata from Upper Triassic to Lower Cretaceous age. The Upper Triassic strata are only seen in the footwall of F1 and F2. Each scenario was investigated following the workflow in Figs. 7 and 8.

4.2.2.1. F1 scenarios. Scenario 1.1 (Fig. 11a) presents F1 as segments F1a and F1b that are disconnected by an open, vertical relay zone. Both segments offset LCU and terminate below H3. The horizon below the

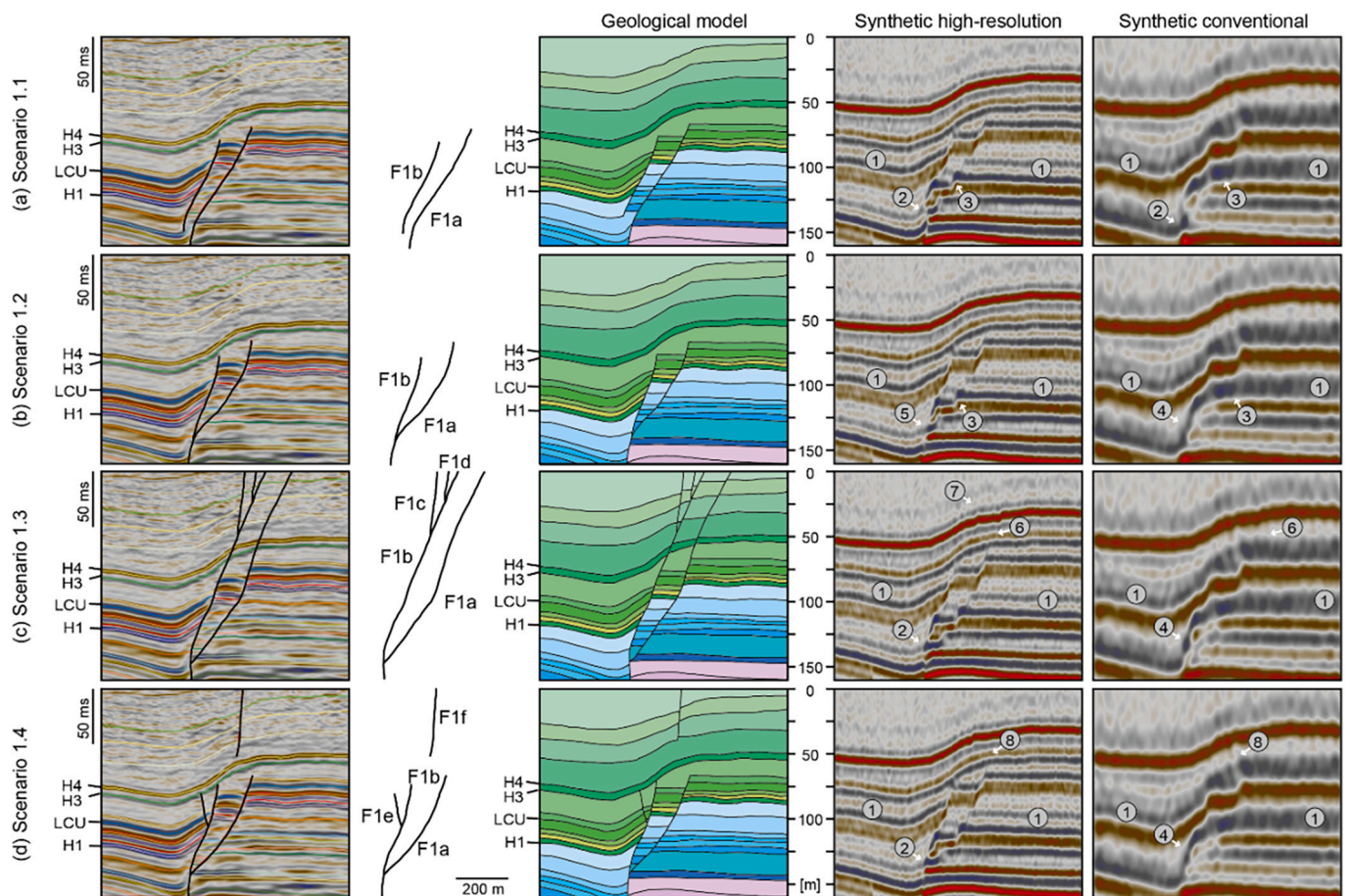


Fig. 11. The result of the hybrid fault interpretations (scenarios) of area 1, fault F1. See location in Fig. 6b. Fault and horizon interpretation on the seismic data in time (first column); Line drawings of the fault geometries for each scenario (second column); Geological layered model in depth (third column); Synthetic high-resolution results (fourth column) and synthetic conventional results (fifth column) in depth. Fig. S2.1 in supplementary material 2 presents all interpretations inside area 1 individually. (a) Scenario 1.1: disconnected fault segments. (b) Scenario 1.2: simple imbricated fan. (c) Scenario 1.3: Complex imbricated fan. (d) Scenario 1.4: Synthetic/antithetic fan. The numbered labels point out key observations described in the text. We utilize the wavelet for 750–850 ms depth interval for the synthetic seismic. The vertical exaggeration (VE) is 5 for the synthetic seismic sections. The applied PSF's are shown in Fig. 10c,d. The horizontal scale is the same for all panels. See text for more details. Seismic data courtesy of TGS, WGP and VBPR.

lower fault tip of F1b is traced to fit the fault geometry. A greater degree of interference is observed in the conventional compared to the high-resolution synthetic seismic section (label 1; Fig. 11a), with 11 reflections in the conventional synthetic seismic corresponding to 20 reflections in the high-resolution synthetic seismic. In both synthetic sections the deeper horizon is offset near the fault tip (label 2; Fig. 11a). This is better expressed in the high-resolution section, where the faults appear to branch even though the geological model shows F1a and F1b as disconnected. The horizons below the F1b fault tip flex towards F1a. For this apparent drag-fold, the conventional synthetic seismic appear with very small throw and a central horizon nearly connects with wall-rock layers (labels 2 and 3; Fig. 11). On the contrary, there are different layers juxtaposed across the fault in the high-resolution synthetic seismic. In this case, there is a distinct fault block bounded by F1a and F1b.

A continuation of scenario 1.1 is a simple imbricated fan (scenario 1.2; Fig. 11b), which matches 12 of the 20 interpretations from the test-panel (Fig. S2.3 in supplementary material 2). In this scenario, the open, vertical relay is now breached by fault F1a curving and connecting with F1b at depth. Further, F1a and F1b terminate slightly shallower compared to scenario 1.1, but this is indiscernible in the synthetic seismic data. There is a slight difference in the deep part of the two scenarios but branching of the segments remains questionable in both (between labels 2 and 3 in Scenario 1.1 and between labels 3 and 4/5 in

Scenario 1.2; Fig. 11a,b). The conventional synthetic seismic is unable to resolve the lower part of the fault block bounded by F1a and F1b. At label 4 in the conventional synthetic seismic section, F1 is represented by a continuous reflection that appears to bend, linking the hanging wall and footwall. Notably, in the conventional synthetic seismic the flexing and apparent continuous reflection could easily be considered a fault tip monocline with intact layers in an open relay between deep and shallow fault tips. This contrasts the isolated layers in the fault block between F1a and F1b as depicted by the high-resolution data for both scenarios 1.1 and 1.2 (Fig. 11a,b).

For scenario 1.3 (Fig. 11c), the imbricated fan has been expanded to shallower levels. Near the upper tip, fault segments F1a and F1b breach the H3 and H4 horizons before terminating in the shallow subsurface at the top of the model. F1b is further segmented into three; the main fault segment F1b connected to two synthetic splays (F1c and F1d). Further, throws for F1c and F1d as well as F1a and F1b are minimal. The H3 and H4 horizons appear intact but flexed in both synthetic seismic sections (label 6; Fig. 11c), without offset as implemented in the geological model. However, reflections in the overlying H4-URU, for instance at label 7, are disturbed and may allow recognition of small throws for the high-resolution synthetic. On a different note, the apparent fault tip monocline discussed in scenario 1.2 (label 4; also better expressed in scenario 1.4, see below), is less prominent and more similar to scenario 1.1. A reason for this may be that the connection of F1a and F1b is

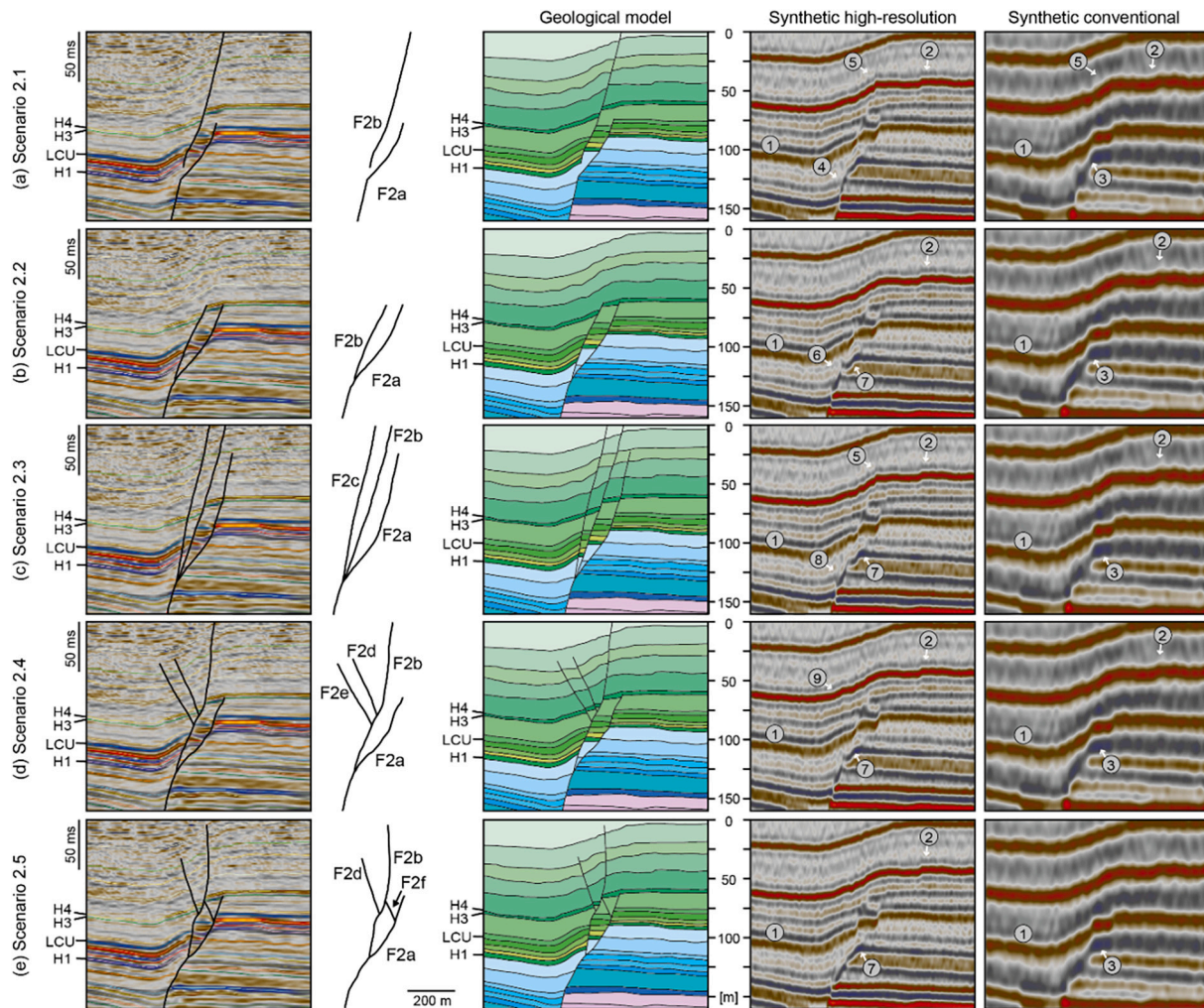


Fig. 12. The result of the hybrid fault interpretations (scenarios) of area 2, fault F2. See location in Fig. 6b. Fault and horizon interpretation on the seismic data in time (first column); Line drawings of the fault geometries for each scenario (second column); Geological layered model in depth (third column); Synthetic high-resolution results (fourth column) and synthetic conventional results (fifth column) in depth. Fig. S2.2 in supplementary material 2 presents all interpretations inside area 2 individually. (a) Scenario 2.1: Disconnected fault segments. (b) Scenario 2.2: Simple imbricated fan. (c) Scenario 2.3: Complex imbricated fan. (d) Scenario 2.4: Complex fan with antithetic reverse fault. (e) Scenario 2.5: Imbricated fan with a fault lens. The numbered labels point out key observations described in the text. We utilize the wavelet for 750–850 ms depth interval for the synthetic seismic. The vertical exaggeration (VE) is 5 for the synthetic seismic sections. The applied PSF's are shown in Fig. 10c,d. The horizontal scale is the same for all panels. See text for more details. Seismic data courtesy of TGS, WGP and VBPR.

deeper (c. 143 m) in the geological model compared to scenarios 1.2 and 1.4 (c. 135 m). Furthermore, the deeper part of the fault block is slightly wider for scenario 1.3. The small difference in offset and thickness can decrease the interference of the reflections and give a better separability of the layers.

Scenario 1.4 (Fig. 11d) explores a combined synthetic (F1a and F1b) fan with an antithetic splay (F1e) and a shallow isolated fault (F1f). This is a combination of scenarios 1.2 and 1.3, with F1a and F1b identical to scenario 1.2. The synthetic seismic sections reveal that F1e is indiscernible in any of them as the small throw is below seismic resolution. In the conventional synthetic seismic section, F1a appears to offset H3-H4 (label 8) while the high-resolution synthetic section shows continuous reflection associated with H3-H4.

4.2.2.2. F2 scenarios. Structural expressions of F2 scenarios as outlined in Fig. 12 show similarities to the F1 scenarios (Fig. 11), but the fault segments vary in length and geometry. In these scenarios, H3 and H4 lack the high-amplitude in the hanging wall as seen in the actual seismic data, but can be used as key horizons to guide different scenarios in the synthetic seismic.

Scenario 2.1 displays the deeper F2a and a shallower F2b that are

disconnected by a vertical open relay (Fig. 12a). Both fault tips curve towards each other in the relay. In the conventional synthetic seismic section there is significant interference where two reflections can be identified compared to five reflections in the high-resolution synthetic seismic section (label 1; Fig. 12a). The gentle disturbance labelled 2 in the conventional synthetic seismic section may look like a fault in the high-resolution synthetic seismic section. In contrast, the geological model does not include a fault in this position. In the relay zone at c. 112 m an apparent continuous curved reflection in the conventional synthetic seismic section (label 3; Fig. 12a) can be interpreted as a fault-tip monocline. This contradicts the high-resolution synthetic seismic section, where several reflections in the hanging wall flex and terminate at F2a (label 4; Fig. 12a). A monocline geometry is expressed in the conventional synthetic sections for all five scenarios and represents the most likely interpretation pitfall associated with F2. F2b offsets the shallowest reflections with a small (2–5 m) throw. Shallower parts of this fault may be picked in high-resolution synthetic section but only shows up as distortions of horizons in the conventional synthetic section (label 5).

Scenario 2.2 (Fig. 12b) tests an imbricated fan in which F2b bifurcates from F2a at depth (c. 125 m), which is similar to scenario 1.2. Fault F2a terminates below H3 while F2b offsets H4. This imbricated fan

is clear in the high-resolution synthetic seismic section (between label 6 and 7; Fig. 12b). F2a and F2b are locally detected in the conventional synthetic seismic section (for all F2 scenarios) but it is not possible to outline the deeper part of the fault block bounded by the two fault segments.

In scenario 2.3, described as a more complex imbricated fan, F1 splays into three fault segments (F2a, F2b and F2c) that cut up-section, nearly to URU (Fig. 12c). Noticeably, both synthetic seismic sections allow recognition of F2a and F2b, while F2c can be traced as a separate segment at depth in the high-resolution synthetic seismic (label 8; Fig. 12c).

Scenario 2.4 is a combination of scenarios 2.2 and 2.3, and in

addition two small antithetic reverse faults (F2e and F2d) cut the H3 to H4 level (Fig. 12d). The two antithetic faults branch with F2b at 75–80 m depth. The apparent reverse faults are considered normal faults that are rotated in the fault tip monocline. F2a terminates below H4 whereas F2b extends to the top of the model. The antithetic faults are indiscernible even in the high-resolution synthetic seismic section but trigger some disturbances in the reflections (label 9; Fig. 12d). In the high-resolution synthetic seismic, the internal layers in the fault block, between F2a and F2b, are well imaged. F2a is imaged below this fault block. For the conventional synthetic seismic, only F2a can be picked with certainty.

In scenario 2.5, a fault lens is bound by segment F2f, in addition to

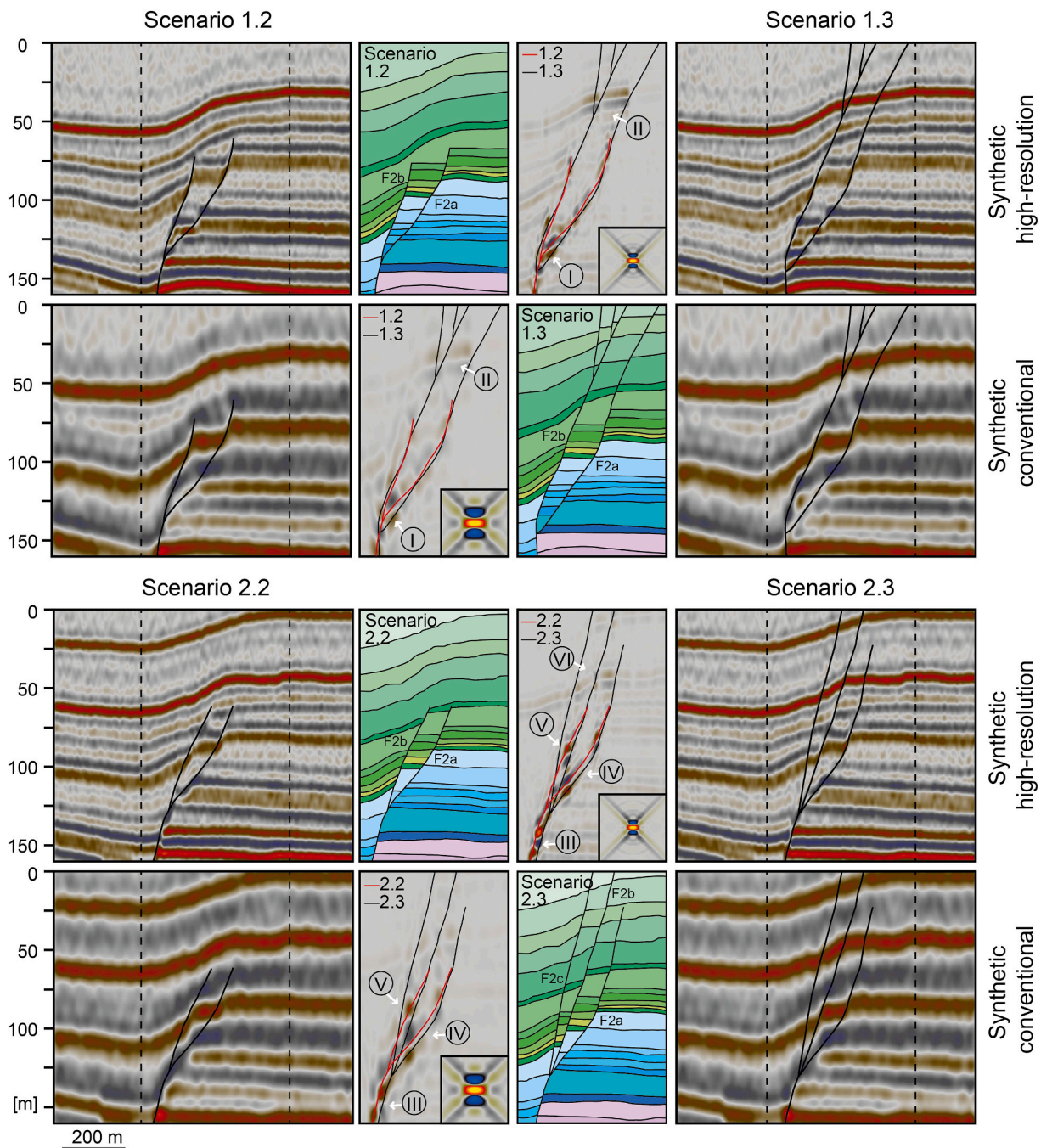


Fig. 13. Scenarios 1.2 vs. 1.3 and 2.2 vs. 2.3 are compared in more detail including difference plots highlighting the difference in synthetic seismic response between the geological fault models/interpretations. The roman numerals in the difference plots point out key observations described in the text. The difference plots are made for both high-resolution and conventional synthetic seismic for each comparison. The vertical exaggeration (VE) is 5 for the synthetic seismic sections, while the PSF's in the difference plot are VE = 1.

fault segments F2a and F2b (Fig. 12e). There is also an antithetic fault, F2d. In this case the antithetic F2d can also not be identified with certainty, especially in the conventional synthetic seismic section. Further, the fault lens is not expressed in the synthetic seismic sections as it is in the geological model. This may be due to F2f only being picked internally in one layer (between LCU-H3), hence it has the same elastic parameters on both sides of the segment, and therefore there is no acoustic impedance contrast and no response in the synthetic seismic sections.

4.2.3. Summary of modelling results

Several observations apply to all fault scenarios (Figs. 10–13): (1) In the high-resolution synthetic seismic sections for the scenarios it is easier to detect minor offsets (3–10 m) in the horizons above the main faulted interval. (2) The down-faulted blocks bounded by the two fault segments (F1a-b and F2a-b) have better spatial resolution in the high-resolution data, in which they appear more isolated and the internal layers are more distinct. (3) The different fault interpretations between the scenarios can mostly be seen in the high-resolution synthetic seismic sections while it remains hard to detect some of the variations in the conventional synthetic seismic sections (Figs. 10–13).

Selected scenarios are compared in more detail including difference plots highlighting the difference in synthetic seismic response between interpretations (Fig. 13). The strong amplitude at depth in the difference plot between scenarios 1.2 and 1.3 result from different location of the connection point of F1a and F1b (label I; Fig. 13). In scenario 1.3, they connect at deeper level and the fault block is wider than in scenario 1.2. The difference in the shallow part (c. 50 m) is due to scenario 1.3 splitting into three segments, which penetrate further up with small offsets of the shallow layers (label II; Fig. 13). The fault geometries in scenarios 2.2 and 2.3 are shifted with respect to each other, and the strong amplitudes at depth in the difference plot are located in between the two fault interpretations (label III; Fig. 13). The same shift can be seen in deeper parts of fault segment F2a giving rise to clear amplitudes in the difference plot (label IV; Fig. 13). This difference is however hard to see in the synthetic seismic sections. There is also a clear difference in the footwall of F2b (label V; Fig. 13). The largest difference is related to the shift of F2b interpretations between the two scenarios. The small offsets of the shallow layers by F2a-c in scenario 2.3 are enough to make a difference in seismic response of the two fault models (label VI; Fig. 13). For scenario 2.3 this can be a potential fluid migration pathway compared to scenario 2.2 – but this is indiscernible in the synthetic seismic section. Similar considerations can be made by comparing the shallow faults in scenario 1.3 to scenario 1.2 (Fig. 13). All differences described above are easier to recognize in the synthetic high-resolution seismic section than in the conventional synthetic seismic. In the synthetic conventional sections, the differences appear more blurred (Fig. 13).

5. Discussion

Our approach to uncertainties associated with seismic interpretation of normal faults is addressed in three steps. First, we discuss objective and subjective uncertainties of the seismic data itself and seismic interpretation before we compare manual and automatic fault interpretations. Following this, we consider the contribution of our seismic modelling approach to improve confidence in seismic interpretation. Finally, we deliberate on uncertainties in interpretations and highlight challenges and pitfalls that may guide the interpreter's work.

5.1. Seismic interpretation uncertainty

Subsurface geology is three-dimensional and detailed mapping requires 3D seismic data. Still, much of the basic seismic interpretation, both of structural and depositional features, are carried out in 2D vertical sections (a combination of inlines, crosslines and arbitrary lines extracted from 3D cubes). An integration of such interpretations,

combined with horizontal sections and 3D interpretation tools, result in 3D models of the subsurface. This study focuses mainly on seismic interpretation of 2D vertical sections from two 3D cubes of different seismic resolution (key profiles in Fig. 3e,f). We address challenges related to limitations associated with imaging of faults in 2D seismic sections, due to uncertainties and interpretation pitfalls. Based on the interpretation of the key profiles, geological models are constructed and tested by seismic modelling to shed light on limitations.

5.1.1. Objective uncertainties

Limitations in 2D and 3D seismic data coupled with 1D boreholes encompass uncertainty that comes with the seismic image (Schaaf and Bond, 2019). Seismic image quality spans geophysical parameters of the seismic acquisition and the subsequent processing (Botter et al., 2014, 2016), as illustrated in Fig. 2. Quality of the seismic data entails the design of the seismic source, receiver ranges and trace density (e.g., Lebedeva-Ivanova et al., 2018), whereas the associated wavelet (with its frequency band) and the unit velocity limit the vertical resolution to $\lambda/4$ and lateral resolution to $\lambda/2$ (Lecomte, 2008; Lebedeva-Ivanova et al., 2018). Accordingly, higher frequency and/or lower velocity provide better resolution but these are not found at greater depths. The high-resolution dataset utilised in this study has frequencies of around 150–200 Hz and extend down to 1150 ms TWT, whereas the conventional 3D data that extend down to 7 s TWT has frequencies of 20–60 Hz. This corresponds to a vertical seismic resolution of 3–7 m for high-resolution seismic data and 15–25 m for conventional seismic data.

The high-resolution P-Cable data are only available for the shallow subsurface, mainly due to rapid attenuation of higher frequencies with depth. The best quality data are derived from above the first seabed multiple in marine seismic data because of challenges related to multiple depression in the short offset P-Cable data (Planke et al., 2010; Lebedeva-Ivanova et al., 2018). In the Hoop area in the SW Barents Sea (study area), the water depth is about 450 m (600 ms TWT), giving room for high-resolution data down to 1200 ms TWT (about 900 m below the seabed). As the structures analysed herein are shallow (upper 500 m below the seabed), attenuation of seismic energy with depth is limited (Brown, 2011). Besides, changes in velocities within the studied depth interval appear moderate (2.2–3.2 km/s), limiting impact of burial related compaction on velocity (Bjørlykke and Jahren, 2015). Resolution and thus imaging-quality generally decreases with depth, accordingly the uncertainties in picking faults increase with depth (Fig. 4 in Schaaf and Bond, 2019).

Seismic processing improves the signal-to-noise ratio (Simm and Bacon, 2014), and can sharpen the shape of the wavelet to improve vertical resolution. Migration techniques improve the seismic image of complex geometries both in terms of vertical and horizontal resolution. Impact of processing is exemplified for our 3D conventional dataset, where recent reprocessing with a smaller sampling interval significantly improved the imaging and resolution at shallow depth (the first 1000 ms TWT; Fig. 2c,d) compared to the dataset utilised by Faleide et al. (2019).

Acquisition provisions with streamer/line spacing and shot point interval determine the bin size. For the conventional data, the bin size of 12.5×18.75 m is the threshold for horizontal resolution in the migrated seismic data, whereas the corresponding threshold for the high-resolution data is constrained by the bin size of 4.7×6.25 m. Source to receiver offset controls the incident angle, which in turn has an impact on the reflectivity and resolution (Lebedeva-Ivanova et al., 2018). Thus, increasing the incident angle decreases the resolution of the seismic image. The conventional dataset in this study has a maximum offset of 6180 m and incident angles typically ranging between 5.1 and 72.1° for a target depth at 1000 m (including 450 m water). For the high-resolution seismic data, the maximum offset is 163 resulting in an incident angle of 3.3°–4.5°. Finally, line orientation (shooting direction) versus structural dip affects imaging. The illumination angle controls what parts of a dipping structure are imaged in the seismic data, and constrains the lateral resolution (Wrona et al., 2020). Angles of

maximum illumination seldom exceed 40–50° dip, thus hampering the imaging of faults. In this study, the deeper parts of F1 and F2 have dips of about 40° (Fig. 10b), which is consistent with the fault plane reflections observed in the synthetic seismic sections in Fig. 10c,d (label 3). The shallower fault segments are steeper, and are not imaged with the given illumination angle (45°), so these are detected as discontinuities along the nearby reflections.

The shadow zone below the two main faults is a potential seismic artefact and interpretation pitfall that adds to the objective uncertainty. This seismic artefact is misinterpreted by many in the test-panel as an antithetic fault below F1a and F2a, which is part of the mean fault model (Fig. 10a,b and Figs. S2.1-S2.2 in supplementary material 2). In this case, there is a link to the interpreters background, as this interpretation seems to be favoured by the non-structural geologists.

Seismic attributes are used to obtain the best detection and imaging of faults and other geological features (Brown, 2011; Botter et al., 2014, 2016; Mondol, 2015). Seismic attributes do not change/improve the objective uncertainty but can be used as a beneficial tool to extract more interpretation details out of the seismic data. In this study, variance is used to investigate important structural features in the study area. In time slices through the variance cube there are discontinuities that likely represent fault zones, including signal disturbances in what could be damage zones, similar to those described by Alaei and Torabi (2017). These zones in the variance cube are up to 60–80 m wide. Given the bin size of the 3D high-resolution seismic data (4.7 × 6.25 m), possible damage zones have been sampled up to ten times across the fault zone. This advocates for possibilities to map damage zones in the shallow subsurface; however, this would likely be more challenging for conventional 3D seismic data with less resolution. Attribute-blending can also be a powerful tool to highlight and interpret different structural and depositional features in seismic data. For fault interpretation, a blend of semblance, dip and tensor attributes is recognised as a good combination (Cunningham et al., 2019).

In this study, uniqueness is found in overlapping conventional and high-resolution seismic data coupled with well data. By comparing the two seismic datasets, we highlight uncertainties that depend on seismic resolution and image quality. Objective uncertainties diminish as vertical resolution improves from 20 m to 5 m between data types. To further test limitations of the seismic data, seismic modelling of 2D geological fault models were applied (see 5.3 below).

5.1.2. Subjective uncertainties

The human bias encountered by different workers manually interpreting faults in seismic data, will influence interpretations and geological models (Bond et al., 2012; Bond, 2015). For instance, faults are best mapped in lines that are perpendicular to the strike of the fault. Human bias is curtailed by geological reasoning and rules that link to attained experience and education as well as current trends in the scientific community (Freeman et al., 2010; Bond et al., 2012, 2015; Alcalde et al., 2017a). In this context, persons in our test-panel are experienced in seismic analysis of faults and/or stratigraphy, hence minimizing bias by experience and insight into concepts. To avoid a framing bias, the conventional seismic data interpretation was conducted prior to the interpretation of the high-resolution seismic data. Manual fault mapping by the test-panel, as illustrated in Fig. 6 and Figs. S2.1-S2.2 in supplementary material 2, is an unconstrained process that generates multiple interpretations per dataset (Bond et al., 2008; Bond, 2015). For the test-panel, it is reasonable to assume that all interpreters conducted their interpretation based on a conceptual model of extensional fault geometries. The differences between the various interpretations must therefore be ascribed to human bias.

We agree with Bond et al. (2007, 2012, 2015) regarding the importance of validating models by considering the geological evolution of the area in light of information from seismic and borehole data. Given the short time allocated for each section in this study, emphasising fault geometries (no horizon interpretation), there is limited critical

validation of interpretations. If the test-panel had more time on the task, coupled with familiarity to the area, they would likely present interpretations that are more robust. A common example of subjectivity is that some interpreters favour picking of faults towards the hanging wall cut-off side, while others prefer the footwall side (Michie et al., 2021; Alcalde et al., 2017b). This variability in fault lines (Fig. 6a,b) influences fault heave (Alcalde et al., 2017b), and can affect subsequent studies of the fault stability (Michie et al., 2021).

For the high-resolution seismic data, less objective uncertainty may have contributed to less subjective uncertainty in the picking of the main faults compared to the interpretation of the conventional seismic data (Fig. 6). On the other hand, the improved resolution of the high-resolution P-Cable data allows identification of smaller-scale features resulting in an overall more intricate interpretation. Most interpreters picked a number of minor faults in the high-resolution data but their interpretations show considerable variations (subjective uncertainties). The up-section fault picking is clearly subjective with a significant spread in location of fault tips (Fig. 6, Figs. S2.1-S2.3 in supplementary material 2). Most fault picks are based on termination/offset of strong reflections and the fault-tips are placed accordingly. Others continue tracing of the faults upwards/downwards into intervals with less reflectivity, partly based on geological reasoning. The choice of fault tips has, for instance, implications for the projected fault-growth history.

5.2. Machine-based automatic seismic interpretation

Human bias can be countered by machine-based interpretation techniques (e.g., Huang et al., 2017; Wu et al., 2018, 2019; Schaaf and Bond, 2019) that follow pre-defined protocols, placing the objective uncertainty as the key challenge. Interpreter #21 was included to test how one method of machine-based automatic fault interpretation performs in comparison to the manual picks of the test-panel (Fig. 9). As each interpreter presents non-unique results through several trials, different algorithms and different trained neural networks will also work differently. However, in the presented case, the same trained network is applied on both the high-resolution and conventional seismic data. This allows objective assessment of impacts derived from input data, demonstrating how the exact same interpretational method produces different results from the two seismic volumes.

The two results of machine-based automatic interpretations are somewhat consistent, showing the two major faults, although the high-resolution results are more detailed, continuous and deeper. Compared to the manual interpretations faults appear more segmented (Fig. 9). This can be explained by the small size of the synthetic cubes used for the unsupervised training of the model, favouring smaller isolated fault segments rather than a major through-going fault. The fault identification appears partly conservative due to a reliance on the termination of strong reflections.

Limitations with machine-based fault identification are related to the training data used to pre-condition the network. Although different reflectivity models, different seismic frequency content and noise, and different types of fault geometries were included in the training data, the synthetic data fail to cover all fault scenarios. For instance, the training data have abrupt reflection terminations, which are not necessarily the case in actual data. Therefore, with improved training data the machine-based fault identification would likely perform better.

5.3. Seismic modelling

Seismic modelling was utilised herein to test the effects of subjective and objective uncertainties, addressing the limitations in resolution and illumination of the seismic data. Most similar studies have targeted outcrop scenarios which are void of errors associated with depth conversion, and provide a high level of details in exposed parts of the outcrop (e.g., Botter et al., 2017; Lecomte et al., 2015; Anell et al., 2016; Kjoberg et al., 2017; Eide et al., 2018; Rabbal et al., 2018; Lubrano-

Lavadera et al., 2018; Wrona et al., 2020). Seismic modelling is integrated to explore the detection threshold of faults in both types of seismic data, as the method highlights the details which may be detected and eventually resolved in different types of seismic data (limit of visibility vs limit of separability). Synthetic seismic sections based on models also incorporating details known from outcrops offer the interpreter guidance around viable geometries in work with actual seismic data.

In this study, the models are based on interpretation of the high-resolution seismic data providing more details than in the conventional data. Still, the level of details in the geological model has limitations (because of the objective and subjective uncertainties of the seismic data). On the other hand, the relevance of the models is secured since they describe the subsurface of the study area. Adding field analogues (outcrops) as basis for detailed geological models will always be questionable regarding the relevance and comparability to the subsurface case. Another challenge relates to establishing relevant petrophysical parameters for the geological model based on outcrop geology. Rock properties of samples from outcrops are rarely representative for a subsurface case, compared to parameters of geophysical logs as available for the study area.

A test of all geophysical parameters applicable to seismic modelling is beyond the scope of this study; as such we use parameters that are appropriate for the two datatypes utilised herein. Different incident angles and wavelets (dominant frequencies; Fig. S1.1 in supplementary material 1) are used for each seismic dataset reflecting their characteristic acquisition parameters and the corresponding resolution (Lebedeva-Ivanova et al., 2018). The same illumination angle of 45° was applied, corresponding to standard seismic illumination (Rabbel et al., 2018).

Previous studies identify significant improvement of the seismic image increasing frequency from 10 to 20 Hz to 30–40 Hz (Botter et al., 2014; Anell et al., 2016). A frequency range of 90–150 Hz, representative for the high-resolution data in this study, reveals a distinct width and internal layering in the down-faulted block (Figs. 10–13). The high-resolution seismic data, through interpretation, depth conversion and model building, form the fundament for the 2(3)D PSF-based convolution seismic modelling that we used to examine fault scenarios herein (Figs. 5 and 7). Subjective interpretation uncertainty (Fig. 6) and objective challenges guided the derived mean geological model (Fig. 10) and the scenarios representing the variability of F1 and F2 interpretations (Figs. 11–13). All interpretations exhibit the two main fault segments (F1a,b in Fig. 11; F2a,b in Fig. 12; Figs. S2.1 and S2.2 in supplementary material 2), while they vary in fault length, position and number of branching points, and the number of smaller fault segments.

The interpretation of fault termination positions are highlighted in scenarios 1.1 and 1.2 (Fig. 11). Here, the fault terminations are placed at different levels within the LCU-H3 interval but these differences are not reflected in the geological layered models and therefore not seen in the synthetic seismic sections. In the models the terminations are linked to a specific horizon and the offset of this horizon provides the criteria for identifying the fault (e.g., Bajorich and Farmer, 1995; Alcalde et al., 2017b). Hence, marker truncations are key, which points to a larger component of subjective criteria in intervals with weak or no reflections. Besides, smaller fault displacements near or below geophysical detection thresholds can in many cases only be noticed by disturbances in otherwise continuous reflections. This creates a significant uncertainty in the outcome of the test-panel's interpretations, and clearly appears as a challenge for the machine-based automatic fault interpretation (Fig. 9). The latter however adjusts the sensitivity to interval signatures, thereby identifying faults that are missed in the manual picks.

Distortion of reflections is a major uncertainty associated with faults, which is especially noticeable in the conventional seismic data (Figs. 10–13). This effect is most prominent between closely spaced fault segments where normal drag of layers towards faults is apparent. Most interpretations produced by the test-panel vary significantly with respect

to choices around open relays or fault branch points (Fig. 6, Figs. 10–12, Figs. S2.1–S2.2 in supplementary material 2). As the geological models show (Figs. 11 and 12), there are clear-cut truncations and limited flexing of beds/horizons. Hence, the distortion of reflections combines a lack of illumination of the fault planes (too steep) coupled with poor lateral resolution of the seismic data. Thereby, proposed fault tip monoclines from vertically segmented faults, albeit seen in nature (e.g., Sharp et al., 2000; Braathen et al., 2011), must be considered with caution in seismic imaging of faults. An interesting point here is that machine-based interpretations of Fig. 9 show more vertically segmented faults. Thereby, this method does not clearly falsify the monocline model.

Noise was added to tentatively match the background pattern of original seismic images, in an approximation of acquisition and processing/imaging noise. The random noise generated for superposition onto the synthetic seismic sections was in addition computed on the same grid (size and sampling) as the geological models, i.e., with a dense sampling of 1 m horizontally and 0.2 m vertically, while the original seismic data are on much coarser grids. This gives a noise model that may offer a higher spatial variability compared to the actual seismic data. In-depth analysis of the noise in actual seismic datasets and improved methods for implementation in synthetic seismic data, could allow additional insight to fault analyses and processing techniques.

6. Summary and conclusions

This study addresses seismic interpretation of faults, highlighting limitations and potential pitfalls due to objective and subjective uncertainties. This knowledge can guide risking workflows that must take account of significant uncertainty in fault models, which is carried forward to fault analysis techniques such as juxtaposition analysis, quantitative fault seal analysis, and fault stability analysis. The main findings are:

- Objective uncertainties decrease when high-resolution seismic data is available in addition to conventional seismic data.
- Subjective uncertainties from human bias will always influence interpretation results; statistical analysis and sorting of fault interpretations shows significant variations between manually picked faults.
- Seismic uncertainties will always be present when working with subsurface data but efforts should be done to minimize their effects on the interpretations. Some efforts have been outlined in this paper.
- Identifying fault tips in seismic data is challenging and smaller antithetic faults are rarely recognizable.
- Masking of closely spaced fault segments by distorted reflection signatures creates apparent extensional fault tip monoclines. This effect is higher for conventional versus high-resolution data.
- Seismic modelling shows which details may be detected and eventually resolved in different types of seismic data.
- Machine-based automatic fault interpretation is void of subjective bias and speeds up initial interpretation significantly, but is still subject to objective uncertainties inherent in seismic data (resolution limitations).
- This study demonstrates how interpretation of high-resolution seismic data, combined with seismic modelling, can increase confidence in the interpretation of conventional data from the same area.

Credit author statement

Faleide: Responsible for conception and design of the work, data collection, data analysis and interpretation; writing, figures, editing and revising the manuscript.

Braathen: Contributed to design and conception of the work, helped in developing and maturing ideas, discussion of results and state of the art, commenting/editing the manuscript.

Lecomte: Advised during the seismic modelling. Commenting/editing manuscript with emphasis on the seismic modelling part.

Mulrooney: Contributed to conception and design of the work. Commenting/ editing manuscript and improving English language.

Midtkandal: Commenting/editing the manuscript.

Bugge: Responsible for performing the machine-based automatic interpretation. Contributed to text related to this part of the work.

Planke: Commenting/editing manuscript with emphasis on seismic data (acquisition, processing, interpretation).

Declaration of Competing Interest

The authors declare that they have no known competing financial interests or personal relationships that could have appeared to influence the work reported in this paper.

Acknowledgements

TGS, WGP and VBPR are greatly acknowledged for providing seismic data. This article is dedicated to COTEC and the NCCS-centre through grants by the Research Council of Norway (295061 and 257579). We appreciate the efforts of the test-panel, the VBPR-team for help and discussion and Thorbjørn Dahlgren (Equinor) for providing important time/depth relation for the Gemini North well. We thank Schlumberger for academic license for Petrel software, NORSAR for academic license for SeisRoX and PETEX for MOVE software available at the University of Oslo. Nestor Cardozo and Charlotte Botter are thanked for thorough and constructive reviews.

Appendix A. Supplementary data

Supplementary data to this article can be found online at <https://doi.org/10.1016/j.tecto.2021.229008>.

References

- Alaei, B., Torabi, A., 2017. Seismic imaging of fault damaged zone and its scaling relation with displacement. *Interpretation* 5. <https://doi.org/10.1190/int-2016-0230.1>.
- Alcalde, J., Bond, C.E., Johnson, G., Butler, R.W.H., Cooper, M.A., Ellis, J.F., 2017a. The importance of structural model availability on seismic interpretation. *J. Struct. Geol.* 97, 161–171. <https://doi.org/10.1016/j.jsg.2017.03.003>.
- Alcalde, J., Bond, C.E., Johnson, G., Ellis, J.F., Butler, R.W.H., 2017b. Impact of seismic image quality on fault interpretation uncertainty. *GSA Today* 27, 4–10. <https://doi.org/10.1130/GSATG282A.1>.
- Alcalde, J., Bond, C.E., Randle, C.H., 2017c. Framing bias: the effect of figure presentation on seismic interpretation. *Interpretation* 5, T591–T605. <https://doi.org/10.1190/INT-2017-0083.1>.
- Anell, I., Lecomte, I., Braathen, A., Buckley, S.J., 2016. Synthetic seismic illumination of small-scale growth faults, paralic deposits and low-angle clinoforms: a case study of the Triassic successions on Edgeøya, NW Barents Shelf. *Mar. Pet. Geol.* 77, 625–639. <https://doi.org/10.1016/j.marpetgeo.2016.07.005>.
- Bahorich, M., Farmer, S., 1995. *The coherence cube*. *Lead. Edge* 1053–1058.
- Bjørlykke, K., 2015. Compaction of sedimentary rocks: Shales, sandstones and carbonates. In: Bjørlykke, K. (Ed.), *Petroleum Geoscience: From Sedimentary Environments to Rock Physics*, Second ed. https://doi.org/10.1007/978-3-642-34132-8_13.
- Bjørlykke, K., Jahren, J., 2015. Sandstones and sandstone reservoirs. In: Bjørlykke, K. (Ed.), *Petroleum Geoscience: From Sedimentary Environments to Rock Physics*. Springer, Berlin Heidelberg, Berlin, Heidelberg, pp. 119–149. https://doi.org/10.1007/978-3-642-34132-8_4.
- Bond, C.E., 2015. Uncertainty in structural interpretation: Lessons to be learnt. *J. Struct. Geol.* 74, 185–200. <https://doi.org/10.1016/j.jsg.2015.03.003>.
- Bond, C.E., Gibbs, A.D., Shipton, Z.K., Jones, S., 2007. What do you think this is? “Conceptual uncertainty” in geoscience interpretation. *GSA Today* 17, 4. <https://doi.org/10.1130/GSAT01711A.1>.
- Bond, C.E., Shipton, Z.K., Gibbs, A.D., Jones, S., 2008. Structural models: Optimizing risk analysis by understanding conceptual uncertainty. *First Break* 26, 65–71. <https://doi.org/10.3997/1365-2397.2008006>.
- Bond, C.E., Philo, C., Shipton, Z.K., 2011. When there isn't a right answer: Interpretation and reasoning, key skills for twenty-first century geoscience. *Int. J. Sci. Educ.* 33, 629–652. <https://doi.org/10.1080/09500691003660364>.
- Bond, C.E., Lunn, R.J., Shipton, Z.K., Lunn, A.D., 2012. What makes an expert effective at interpreting seismic images? *Geology* 40, 75–78. <https://doi.org/10.1130/G32375.1>.

- Bond, C.E., Johnson, G., Ellis, J.F., 2015. Structural model creation: the impact of data type and creative space on geological reasoning and interpretation. *Geol. Soc. Spec. Publ.* 421, 83–97. <https://doi.org/10.1144/SP421.4>.
- Botter, C., Cardozo, N., Hardy, S., Lecomte, I., Escalona, A., 2014. From mechanical modeling to seismic imaging of faults: a synthetic workflow to study the impact of faults on seismic. *Mar. Pet. Geol.* 57, 187–207. <https://doi.org/10.1016/j.marpetgeo.2014.05.013>.
- Botter, C., Cardozo, N., Hardy, S., Lecomte, I., Paton, G., Escalona, A., 2016. Seismic characterisation of fault damage in 3D using mechanical and seismic modelling. *Mar. Pet. Geol.* 77, 973–990. <https://doi.org/10.1016/j.marpetgeo.2016.08.002>.
- Botter, C., Cardozo, N., Lecomte, I., Rotevatn, A., Paton, G., 2017. The impact of faults and fluid flow on seismic images of a relay ramp over production time. *Pet. Geosci.* 23, 17–28. <https://doi.org/10.1144/petgeo2016-027>.
- Braathen, A., Tveranger, J., Fossen, H., Skar, T., Cardozo, N., Semshaug, S.E., Bastesen, E., Sverdrup, E., 2009. Fault facies and its application to sandstone reservoirs. *Am. Assoc. Pet. Geol. Bull.* 93, 891–917. <https://doi.org/10.1306/03230908116>.
- Braathen, A., Bælum, K., Maher, H., Buckley, S.J., 2011. Growth of extensional faults and folds during deposition of an evaporite-dominated half-graben basin; the Carboniferous Billefjorden Trough, Svalbard. *Nor. Geol. Tidsskr.* 91, 137–161.
- Brown, A.R., 2011. Structural interpretation. In: *Interpretation of Three-Dimensional Seismic Data*. Society of Exploration Geophysicists and American Association of Petroleum Geologists, pp. 61–102. <https://doi.org/10.1190/1.9781560802884.ch3>.
- Cartwright, J., Huuse, M., 2005. 3D seismic technology: the geological “Hubble”. *Basin Res.* 17, 1–20. <https://doi.org/10.1111/j.1365-2117.2005.00252.x>.
- Childs, C., Manzocchi, T., Walsh, J.J., Bonson, C.G., Nicol, A., Schöpfer, M.P.J., 2009. A geometric model of fault zone and fault rock thickness variations. *J. Struct. Geol.* 31, 117–127. <https://doi.org/10.1016/j.jsg.2008.08.009>.
- Cohen, K.M., Finney, S.C., Gibbard, P.L., Fan, J.X., 2013. *The ICS international chronostratigraphic chart*. *Episodes* 36, 199–204.
- Collanega, L., Massironi, M., Breda, A., Kjøllhamar, B.E., 2017. Onset of N-Atlantic rifting in the Hoop Fault Complex (SW Barents Sea): an orthorhombic dominated faulting? *Tectonophysics* 706–707, 59–70. <https://doi.org/10.1016/j.tecto.2017.04.003>.
- Cunningham, J., Cardozo, N., Townsend, C., Iacopini, D., Wærum, G.O., 2019. Fault deformation, seismic amplitude and unsupervised fault facies analysis: Snøhvit Field, Barents Sea. *J. Struct. Geol.* 118, 165–180. <https://doi.org/10.1016/j.jsg.2018.10.010>.
- Eide, C.H., Schofield, N., Lecomte, I., Buckley, S.J., Howell, J.A., 2018. Seismic interpretation of sill complexes in sedimentary basins: Implications for the sub-sill imaging problem. *J. Geol. Soc. Lond.* 175, 193–209. <https://doi.org/10.1144/jgs2017-096>.
- Faleide, T.S., Midtkandal, I., Planke, S., Corseri, R., Faleide, J.I., Serck, C.S., Nystuen, J.P., 2019. Characterisation and development of Early Cretaceous shelf platform deposition and faulting in the Hoop area, southwestern Barents Sea-constrained by high-resolution seismic data. *Nor. J. Geol.* 99, 1–20. <https://doi.org/10.17850/njg99-3-7>.
- Fitriyanto, A., 2011. *Structural Analysis of the Hoop Fault Complex, SW Barents Sea*. MSc Thesis. University of Oslo, 93p.
- Freeman, B., Boulton, P.J., Yielding, G., Menpes, S., 2010. Using empirical geological rules to reduce structural uncertainty in seismic interpretation of faults. *J. Struct. Geol.* 32, 1668–1676. <https://doi.org/10.1016/j.jsg.2009.11.001>.
- Gabrielsen, R.H., Færseth, R.B., Jensen, L.N., Kalheim, J.E., Riis, F., 1990. Structural elements of the Norwegian continental shelf. Part I: the Barents Sea Region. *Nor. Petroleum Dir. Bull.* 6, 1–33.
- Hale, D., 2013. Methods to compute fault images, extract fault surfaces, and estimate fault throws from 3D seismic images. *Geophysics* 78, 33–43.
- Herron, D.A., 2011. Resolution. In: Latimer, R.B. (Ed.), *First Steps in Seismic Interpretation*. Society of Exploration Geophysicists, pp. 75–82.
- Huang, L., Dong, X., Clew, T.E., 2017. A scalable deep learning platform for identifying geologic features from seismic attributes. *Lead. Edge* 36, 249–256. <https://doi.org/10.1190/le36030249.1>.
- Kjøberg, S., Schmiedel, T., Planke, S., Svensen, H.H., Millett, J.M., Jerram, D.A., Galland, O., Lecomte, I., Schofield, N., Haug, Ø.T., Helseth, A., 2017. 3D structure and formation of hydrothermal vent complexes at the Paleocene-Eocene transition, the Møre Basin, mid-Norwegian margin. *Interpretation* 5, SK65–SK81. <https://doi.org/10.1190/INT-2016-0159.1>.
- Lebedeva-Ivanova, N., Polteau, S., Bellwald, B., Planke, S., Berndt, C., Stokke, H.H., 2018. Toward one-meter resolution in 3D seismic. *Lead. Edge* 37, 818–828. <https://doi.org/10.1190/le37110818.1>.
- Lecomte, I., 2008. Resolution and illumination analyses in PSDM: a ray-based approach. *Lead. Edge* 27, 650–663. <https://doi.org/10.1190/1.2919584>.
- Lecomte, I., Lavadera, P.L., Anell, I., Buckley, S.J., Schmid, D.W., Heeremans, M., 2015. Ray-based seismic modeling of geologic models: Understanding and analyzing seismic images efficiently. *Interpretation* 3, SAC71–SAC89. <https://doi.org/10.1190/INT-2015-0061.1>.
- Lecomte, I., Lavadera, P.L., Botter, C., Anell, I., Buckley, S.J., Eide, C.H., Grippa, A., Mascolo, V., Kjøberg, S., 2016. 2(3)D convolution modelling of complex geological targets beyond – 1D convolution. *First Break* 34, 99–107.
- Lubrano-Lavadera, P., Senger, K., Lecomte, I., Mulrooney, M.J., Kühn, D., 2018. Seismic modelling of metre-scale normal faults at a reservoir-cap rock interface in Central Spitsbergen, Svalbard: implications for CO2 storage. *Nor. J. Geol.* 99, 329–347. <https://doi.org/10.17850/njg003>.
- Mascolo, V., Lecomte, I., 2020. Seismic modelling of outcrop carbonate systems: An application to the Cretaceous platform-to-basin system of the Maiella Mountain (central Apennines, Italy). In: *Geol. Soc. London, Spec. Publ.* SP509–2019–81. <https://doi.org/10.1144/sp509-2019-81>.

- Michie, E.A.H., Mulrooney, M.J., Braathen, A., 2021. Fault interpretation uncertainties using seismic data, and the effects on fault seal analysis: a case study from the Horda Platform, with implications for CO₂ storage. *Solid Earth* 12, 1259–1286. <https://doi.org/10.5194/se-12-1259-2021>.
- Midtkandal, I., Faleide, J.L., Faleide, T.S., Serck, C.S., Planke, S., Corseri, R., Dimitriou, M., Nystuen, J.P., 2019. Lower Cretaceous Barents Sea strata: epicontinental basin configuration, timing, correlation and depositional dynamics. *Geol. Mag.* 1–19 <https://doi.org/10.1017/s0016756819000918>.
- Misra, A.A., Mukherjee, S., 2018. Seismic structural analysis. In: Misra, A.A., Mukherjee, S. (Eds.), *Atlas of Structural Geological Interpretation from Seismic Images*. Wiley Blackwell, Oxford, pp. 44–46. Chapter 7. ISBN: 9781119158325.
- Mondol, N.H., 2015. Well logging: Principles, applications and Uncertainties. In: Bjørlykke, K. (Ed.), *Petroleum Geoscience*. Springer, Berlin Heidelberg, Berlin, Heidelberg, pp. 385–425. https://doi.org/10.1007/978-3-642-34132-8_16.
- Norwegian Petroleum Directorate FactPages, 2021 [online] Available at: <https://factpages.npd.no/>.
- Planke, S., Berndt, C., Mienert, J., Bünz, S., Eriksen, F.N., Eriksen, O.K., 2010. P-Cable: New High-Resolution 3D Seismic Acquisition Technology. *EGU Gen. Assem. Conf. Abstr.* 12, p. 13618.
- Rabbal, O., Galland, O., Mair, K., Lecomte, I., Senger, K., Spacapan, J.B., Manceda, R., 2018. From field analogues to realistic seismic modelling: a case study of an oil-producing andesitic sill complex in the Neuquén Basin, Argentina. *J. Geol. Soc. Lond.* 175, 580–593. <https://doi.org/10.1144/jgs2017-116>.
- Ronneberger, O., Fischer, P., Brox, T., 2015. U-net: convolutional networks for biomedical image segmentation. *Lect. Notes Comput. Sci. (including Subser. Lect. Notes Artif. Intell. Lect. Notes Bioinformatics)* 9351, 234–241. https://doi.org/10.1007/978-3-319-24574-4_28.
- Schaaf, A., Bond, C.E., 2019. Quantification of uncertainty in 3-D seismic interpretation: implications for deterministic and stochastic geomodeling and machine learning. *Solid Earth* 10, 1049–1061. <https://doi.org/10.5194/se-10-1049-2019>.
- Serck, C.S., Faleide, J.L., Braathen, A., Kjøllhamar, B., Escalona, A., 2017. Jurassic to Early Cretaceous basin configuration(s) in the Fingerdjupet Subbasin, SW Barents Sea. *Mar. Pet. Geol.* 86, 874–891. <https://doi.org/10.1016/j.marpetgeo.2017.06.044>.
- Sharp, I.R., Gawthorpe, R.L., Underhill, J.R., Gupta, S., 2000. Fault-propagation folding in extensional settings: examples of structural style and synrift sedimentary response from the Suez rift, Sinai, Egypt. *Bull. Geol. Soc. Am.* 112, 1877–1899. [https://doi.org/10.1130/0016-7606\(2000\)112<1877:FPFIES>2.0.CO;2](https://doi.org/10.1130/0016-7606(2000)112<1877:FPFIES>2.0.CO;2).
- Shuey, R.T., 1985. Simplification of the Zoeppritz equations. *Geophysics* 50, 609–614. <https://doi.org/10.1190/1.1441936>.
- Simm, R., Bacon, M., 2014. Seismic processing issues. In: Simm, R., Bacon, M. (Eds.), *Seismic Amplitude: An Interpreter's Handbook*. Cambridge University Press, Cambridge, pp. 110–124. <https://doi.org/10.1017/CBO9780511984501.007>.
- Tannert, C., Elvers, H., Jandrig, B., 2007. The ethics of uncertainty. *EMBO Rep.* 8, 892–896. <https://doi.org/10.1038/sj.embor.7401072>.
- Wibberley, C.A.J., Yielding, G., Di Toro, G., 2008. Recent advances in the understanding of fault zone internal structure: a review. *Geol. Soc. Spec. Publ.* 299, 5–33. <https://doi.org/10.1144/SP299.2>.
- Wood, A.M., Paton, D.A., Collier, R.E.L., 2015. The missing complexity in seismically imaged normal faults: What are the implications for geometry and production response? In: Richards, F.L., Richardson, N.J., Rippington, S.J., Wilson, R.W., Bond, C.E. (Eds.), *Industrial Structural Geology*, vol. 421. Geological Society, London, Special Publication, pp. 213–230.
- Wrona, T., Fossen, H., Lecomte, I., Eide, C.H., Gawthorpe, R.L., 2020. Seismic expression of shear zones: insights from 2-D point-spread-function based convolution modelling. *J. Struct. Geol.* 140, 104121. <https://doi.org/10.1016/j.jsg.2020.104121>.
- Wu, X., Shi, Y., Fomel, S., Liang, L., 2018. Convolutional neural networks for fault interpretation in seismic images. In: 2018 SEG Int. Expo. Annu. Meet. SEG, 2018, pp. 1946–1950. <https://doi.org/10.1190/segam2018-2995341.1>.
- Wu, X., Liang, L., Shi, Y., Fomel, S., 2019. FaultSeg3D: using synthetic data sets to train an end-to-end convolutional neural network for 3D seismic fault segmentation. *Geophysics* 84, IM35–IM45. <https://doi.org/10.1190/geo2018-0646.1>.
- Zhao, T., Mukhopadhyay, P., 2018. A fault-detection workflow using deep learning and image processing. In: Presented at the 88th Annual International Meeting, SEG, Expanded Abstract, pp. 1966–1970.